KLOE Note 208
January 13, 2006

Measurement of the branching fraction and the charge asymmetry for the decay $K_S \to \pi e \nu$

C. Gatti and T. Spadaro

Laboratori Nazionali di Frascati - INFN

Abstract

This memo is an update of previous note and Theses on the measurement of the branching ratio and charge asymmetry for the decay $K_S \to \pi e \nu$. Many things have changed: the MC simulation; the selection cuts; the fit procedure. All these items are here discussed. We also include the measure of the form factor slope λ_+.

Contents

1 Introduction **3**

2 New selection **4**
2.1 DATA sample 4
2.2 Selection and new TOF cut 4

3 Efficiency determination **11**
3.1 Analysis scheme: $\sum_n T_n \times P_n$ 11
3.2 K_L-crash simulation 13
3.3 Smearing of MC resolutions for track momenta 17
3.4 Smearing of MC resolutions for cluster times 24
3.4.1 **"Pezzetto" and "Datizza"** 24
3.4.2 **The "Smirizza" procedure** 26
3.5 Tof and trigger-sector efficiencies and T_0 distribution 29
3.6 Cosmic Veto efficiency 36

4 Event counting: new fit procedure **38**
4.1 Definition of the fit procedure 38
4.1.1 **Fit procedure** 43
4.1.2 **Shape correction** 44
4.2 Systematic uncertainties 49
4.3 Determination of the form factor slope parameter λ_+ 54

5 Results **60**
5.1 Interpretation of the results 68

6 V_{us} determination **74**

1 Introduction

This note is an update of the older note [18] and of two PHD Theses [16, 26], where the selection criteria of $K_S \to \pi e \nu$ decays, the analysis scheme, and the selections of the control samples for the evaluation of the selection efficiencies have been accurately described. One of the most important differences with respect to the measurement outlined in [16] is the introduction in the Monte Carlo (MC) the simulation of the radiated photon in the Ke3 final state, as discussed in Ref. [14, 15]. The inclusion of the radiation increased our result by about 3% as discussed in Ref. [25]. Since then, a drastic change in the MC tracking and timing resolutions forced us to change the signal selection and increase the rejection of the background events. Another important difference is in the MC simulation of K_L interactions in the calorimeter. In the old analysis we didn't relay on the MC simulation, but we weighted the kinematic distributions of the generated K_L's with the angular distributions of K_{crash} measured from data. However, an improved MC simulation of K_L interactions allowed us to relay on the simulation, and so to take into account the correlations between K_S and late-K_L decays.

In the following sections we describe the new selection cuts, Sec. 2, together with the evaluation of the related efficiencies, Sec 3. A new scheme for the tag-bias evaluation is described that is used also for the measurement of the ratio $\mathrm{BR}(K_S \to \pi^+\pi^-(\gamma))$/-$\mathrm{BR}(K_S \to \pi^0\pi^0)$. In Sec. 2 we also describe the criteria used to chose our data sample.

The main contribution to background events is given by $K_S \to \pi^+\pi^-(\gamma)$ decays. We investigated all the possible topologies of these events that pass our selection cuts. Each of these topologies can be identified using properly chosen kinematic variables, such as the momentum in the kaon rest frame, the impact parameter of the two tracks etc.. Due to different efficiencies in data and MC the relative abundance of the different topologies is not reproduced in the simulation. Hence, we implemented a fit procedure, described in Sec. 4, in which the amount of signal and of all the topologies of background are left as free parameters.

In Sec. 4 we also evaluate the systematic error and in Sec. 5 and Sec. 6 we give the result for the branching ratio, the charge asymmetry, and V_{us} respectively.

2 New selection

2.1 DATA sample

We performed the measurement of the $K_S \to \pi e \nu$ branching ratio and charge asymmetry on the data collected during the years 2001 and 2002. We divided the whole statistics into 94 periods for a total of about 410 pb^{-1}, as shown in Fig. 1 and in Tabs. 1, 2, and 3. We chose the periods in order to have homogeneous conditions and about 5 pb^{-1} of integrated luminosity per period. First, we grouped consecutive runs with the same $\sqrt{s}$ (within the errors). We discarded those events where the information on the center of mass energy and ϕ momentum and decay position are missing. Also the events with bad trigger conditions have been rejected. Then, we grouped together the events with same trigger conditions. In particular the introduction of the T3 filter has been taken into account, separating the runs with and without T3. We also grouped the runs from 21838 to 22195 into separated periods, since these are affected by a wrong calibration of the calorimeter time scale. All of the efficiencies are evaluated separately for each of the 94 periods. A further grouping into macro-periods was necessary to reach enough statistics for the fit procedure used to count the number of K_{e3} events, discussed in section 4. The 17 macro-periods are listed in Tabs. 1, 2, and 3. The analysis result for the macro-periods is discussed in Sec. 4. This is used only for checks of the result stability, and for systematic checks on the efficiency variation as a function of the period, while the final result is obtained separating the statistics in the year 2001 and 2002. The results obtained with this two methods are compatible as discussed in Sec. 4.

2.2 Selection and new TOF cut

In order to improve the agreement between data and MC, and to reduce the correlation between the number of signal and background events, obtained from the fit to the $E_{miss} - p_{miss}$ distribution, we changed some of the already existing cuts, and added a new ToF cut that rejects about 90% of the residual $K_S \to \pi^+\pi^-$ events. The K_L-crash energy cut has been raised from 100 MeV to 200 MeV. This requirement, increasing the resolution on the estimated K_S momentum, reduces the systematic error as discussed in Sec. 4. We cut on the vertex transverse position, $\rho_{vtx} < 15$ cm [1]. This cut rejects mainly $K_S \to \pi^+\pi^-$ events with a pion decaying to muon and neutrino before the DC. A new cut on the missing momentum has also been added: $P_{miss} > 40$ MeV. This cut rejects background in a kinematic region where the signal is absent. The old ToF cuts have been tuned, increasing

[1] In Ref. [16] we reported the cut $\rho_{vtx} < 4$ cm. However, we later found out that this cut was not applied.

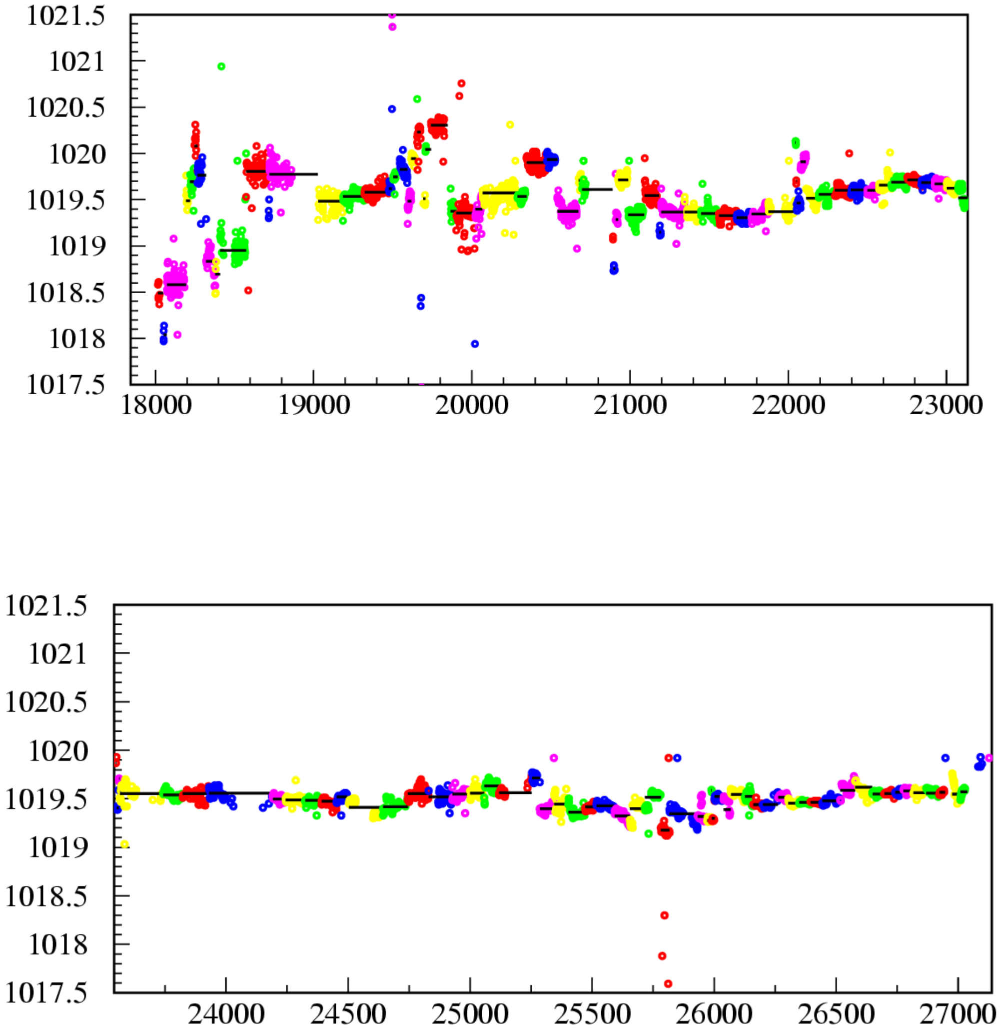

Figure 1: $\sqrt{s}$ as a function of the run number for the year 2001 and 2002. The 94 data periods are shown with different colors.

Period	First Run	Last Run	Macro-period	Luminosity (nb^{-1})
1	17845	18195	1	1594
2	18196	18322	1	365
3	18323	18574	1	599
4	18575	19028	1	7359
5	19029	19247	1	5021
6	19248	19373	1	4802
7	19374	19648	2	7953
8	19655	19847	2	3974
9	19866	20056	2	5758
10	20057	20345	2	6737
11	20346	20540	2	6588
12	20541	20674	2	4305
13	20675	20988	3	3088
14	20989	21174	3	4855
15	21196	21359	3	5197
16	21360	21526	3	8054
17	21527	21617	3	4826
18	21618	21707	3	4440
19	21708	21837	3	5779
20	21838	22044	4	5403
21	22045	22111	4	4876
22	22112	22195	4	5452
23	22196	22301	5	4734
24	22302	22400	5	5098
25	22401	22497	5	4999
26	22498	22573	5	5307
27	22574	22645	5	4461
28	22646	22737	5	4565
29	22738	22827	5	5613
30	22828	22942	6	7094
31	22943	23027	6	5337
32	23028	23133	6	7891

Table 1: Description of the run periods of the year 2001.

Period	First Run	Last Run	Macro-period	Luminosity (nb^{-1})
33	23542	23549	7	131
34	23550	23551	7	38
35	23552	23561	7	667
36	23562	23564	7	178
37	23565	23743	7	5009
38	23744	23822	7	5087
39	23823	23930	8	5033
40	23931	24191	8	5068
41	24192	24244	8	5008
42	24245	24324	8	5067
43	24325	24391	8	5081
44	24392	24452	8	5004
45	24453	24497	9	3495
46	24498	24503	9	70
47	24504	24642	9	5034
48	24643	24744	9	5079
49	24745	24829	9	5029
50	24830	24926	9	5036
51	24927	25000	10	5027
52	25001	25057	10	5115
53	25058	25118	10	5014
54	25119	25252	10	1924
55	25253	25285	10	1546
56	25286	25345	10	5031
57	25346	25402	11	5002
58	25403	25470	11	5052
59	25471	25517	11	5022
60	25518	25592	11	5083
61	25593	25654	11	5013
62	25655	25716	11	5018
63	25717	25781	12	4654
64	25782	25816	12	2171

Table 2: Description of the run periods of the year 2002.

Period	First Run	Last Run	Macro-period	Luminosity (nb^{-1})
65	25817	25932	12	5005
66	25933	25970	12	5113
67	25971	25988	12	895
68	25989	25990	12	235
69	25991	26001	13	1420
70	26002	26037	13	5065
71	26038	26067	13	1765
72	26068	26125	13	5099
73	26126	26159	13	5081
74	26160	26198	13	5032
75	26199	26261	14	5029
76	26262	26303	14	5068
77	26304	26347	14	5150
78	26348	26395	14	5009
79	26396	26442	14	5148
80	26443	26516	14	5183
81	26517	26577	15	5035
82	26578	26647	15	5026
83	26648	26696	15	5085
84	26697	26741	15	5038
85	26742	26775	15	5159
86	26776	26815	15	5076
87	26816	26868	16	5105
88	26869	26921	16	5058
89	26922	26946	16	2989
90	26947	26957	16	1014
91	26958	26975	16	1090
92	26976	27037	16	8985
93	27038	27071	17	4607
94	27072	27137	17	6482

Table 3: Description of the run periods of the year 2002.

$E_{crash} > 200$ MeV
$\rho_{vtx} < 15$ cm
$\lvert z_{vtx} \rvert < 10$ cm
$\rho_{first} < 41$ cm
$22^\circ < \theta_{trk} < 158^\circ$
$\lvert P_S \rvert < 325$ MeV/c
300 MeV $< M_{\pi\pi} < 490$ MeV
$P_{miss} > 40$ MeV
$\lvert d\delta_{t,\pi\pi} \rvert > 1.7$ ns
$\lvert d\delta_{t,\pi e} \rvert < 1.4$ ns and $\lvert d\delta_{t,e\pi} \rvert > 3.2$ ns OR $(\pi \rightleftharpoons e)$
$[(dt_e - 0.1 \text{ ns})/0.4 \text{ ns}]^2 + [(dt_\pi - 0.1 \text{ ns})/0.4 \text{ ns}]^2 < 1$

Table 4: Summary of the selection cuts. See Sec. (4.1) of Ref. [16] for a full description of the selection.

the rejection power of the $d\delta_{t,\pi\pi}$ cut, and loosening the cut on $d\delta_{t,\pi e}$. The selection cuts are summarized in Tab. 4.

The new cut we apply is done by rephasing the cluster times with the global $T0$ of the event, using the clusters of the particles selected as pion and electron:

$$T0 = \mathrm{N}int \left(\frac{dt_\pi + dt_e}{2T_{\mathrm{bunch}}} \right),$$

where:

$$dt_i = T_{cl}(i) - \frac{L_i}{\beta(m(i))c}, \quad i = e, \pi.$$

The cut is shown in Fig. 2 for MC events. A small offset $T_{\mathrm{o}ff} = 0.1$ ns is subtracted to both pion and electron times to center the distribution to zero. The last line of Tab. 4 describes the cut applied.

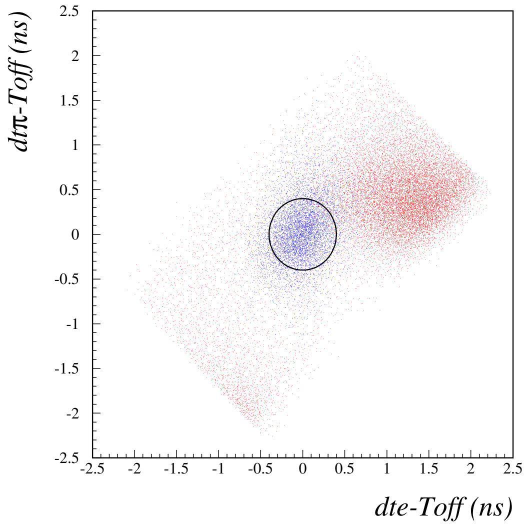

Figure 2: dt_π vs dt_e for MC events, for signal (blue) and background (red) events. The black circle shows the selection cut.

3 Efficiency determination

3.1 Analysis scheme: $\sum_n T_n \times P_n$

In the old version of the analysis scheme we didn't rely on the MC simulation of the kaon interactions in the calorimeter. The angular distribution of the K_{crash} was measured from a data sample of $K_S \to \pi^+\pi^-$ events and then used in the MC simulation to weight the events in which a K_L had reached the calorimeter [16]. However, by using this procedure we didn't include in our MC sample late-K_L in-flight decays mimicking a K_L-crash.

K_L decays before the calorimeter can interfere with the reconstruction of K_S tracks and clusters. We performed a study on the tracking efficiency: we measured the single-particle efficiency for data, using $K_S \to \pi^+\pi^-$ events tagged with a K_L-crash-cluster of 100 MeV to 300 MeV of minimum energy. In the former case the sample includes the contribution of late-K_L decays, contrary to the latter case. We made the ratio of data and MC efficiencies for the two different K_L-crash energy cuts, where for the MC we evaluated the efficiencies with the old procedure, i.e. no late K_L decays. We observed a 0.3% difference in the plateau values of the two ratios of efficiencies, that we can ascribe to the tracking interference. The effect on the branching ratio measurement could be doubled whether the loss is correlated or not between the two tracks. Other correlations arise between the energy, the angular position and the resolution in the estimated K_S momentum. All these effects were not taken correctly into account in the old analysis scheme.

For these reasons, the MC simulation of kaon interactions in the calorimeter has been tuned to reproduce the distributions observed in the data for the arrival time, the energy distribution, and to reproduce the same cross section. This item is discussed in Sec. 3.2.

With the introduction of the K_L-crash simulation in our analysis, we have also modified the method used to evaluate the efficiency corrections and, consequently, our analysis scheme. First of all, we don't need anymore to weight the generated K_L distribution with the measured K_L-crash angular distribution. Second, the position of the T_0 requirement in the chain of the conditional probabilities with which we build the efficiency correction must be changed.

In fact, the T_0 is needed to fix the initial time of the event and the very definition of K_L-crash depends on it. In the logic of the old analysis, sketched in Fig. 3, the T_0 efficiency is evaluated after the tracks are associated to calorimeter clusters, this being the only way we are able to do it for data. On the other hand, the acceptance is evaluated before the T_0-requirement, and the two efficiencies are clearly correlated. However, in the old MC simulation no explicit T_0 requirement was needed for the K_L-crash, and the acceptance could be evaluated independently from the T_0. In the new MC, we have a *true*

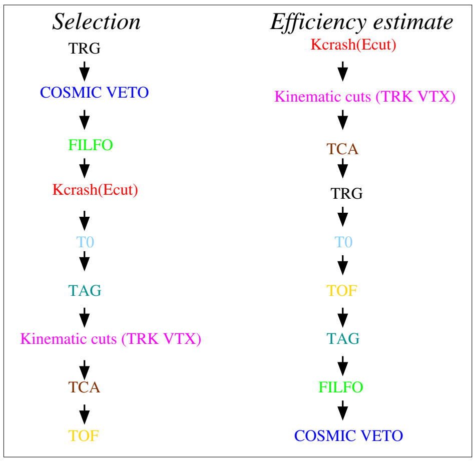

Figure 3: Sequence of the requirements for the $K_S \to \pi e \nu$ selection (left). Each term corresponds to a conditional probability. The order of the cuts is different for the efficiency estimate (right). The product remains the same if each efficiency is estimated using the proper conditions.

K_L-crash in each event and this requires a T_0.

We overcame this problem by defining in the MC a *true-K_L-crash* event, as an event which has a K_L-crash when the T_0 is the correct one, i.e. the one corresponding to the ϕ decay. All the other events are classified as *non-K_L-crash*. All the MC efficiencies are then evaluated separately for true- and non-K_L-crash events, and then combined together using the following formula:

$$\epsilon_{sel} = \epsilon_{Kcr} a_{Kcr} \sum_n T_n P_n^{in} + (1 - \epsilon_{Kcr}) a_{NKcr} \sum_n T_n P_n^{out}, \qquad (1)$$

where ϵ_{Kcr} is the true-K_L-crash efficiency, a_{Kcr} (a_{NKcr}) is the acceptance of a true-(non-)K_L-crash event, P_n^{in} (P_n^{out}) is the probability for true-(non-)K_L-crash event to have a K_L-crash when the T_0 is shifted by n bunches, and T_n is the T_0 distribution, i.e. the fraction of events in which the T_0 is shifted by n bunches. The ratio of $\pi\pi$ and $\pi e \nu$ efficiencies calculated with Eq. (1) already incorporate the tag bias, and the result in Eq. (113) of Ref. [18] is restored if $a_{Kcr} = a_{NKcr}$.

3.2 K_L-crash simulation

A detailed study comparing data with the new MC has been carried on, in order to check the reliability of the simulation in reproducing the angular distribution of K_L crash clusters. Sample of $K_S \to \pi^+\pi^-$ events are used (K_L-tags), in which a K_L-crash is also required. The K_S momentum $\mathbf{P}_S$ is obtained summing the pion momenta at the K_S vertex; the K_L momentum is then obtained as $\mathbf{P}_L^{\mathrm{F}S} = -\mathbf{P}_S + \mathbf{P}_\phi$. The position z_ϕ of the ϕ vertex along the z axis is also calculated intersecting $\mathbf{P}_S$ with the plane $y = \langle y_\phi \rangle$, where $\langle y_\phi \rangle$ is the average y position of the interaction point known from Bhabha events on a run-by-run basis. The direction of $\mathbf{P}_L^{\mathrm{F}S}$ is compared with that of $\mathbf{P}_L^{CR} = \mathbf{r}_L - \mathbf{r}_\phi$, where $\mathbf{r}_L$ is the position of the K_L-crash cluster and $\mathbf{r}_\phi = (\langle x_\phi \rangle, \langle y_\phi \rangle, z_\phi)$ of the ϕ vertex.

Two variables are considered for data or MC, namely the angular differences $\delta\theta$ and $\delta\phi$ between these two vectors in the ρ-z and x-y planes, respectively. The distribution of $\delta\theta$ ($\delta\phi$) is fit with a gaussian in slices of the K_L emission angle θ (ϕ); the standard deviations of these fits are shown in Fig. 4.

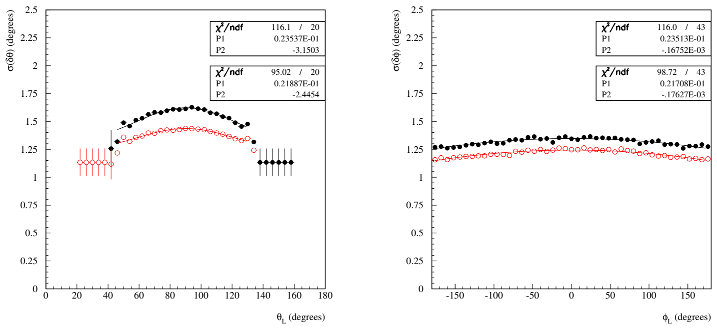

Figure 4: Left (right) panel: standard deviation estimated from gaussian fits of the difference between $\mathbf{P}_L^{\mathrm{F}S}$ and $\mathbf{P}_L^{CR}$ in the ρ-z (x-y) plane, as a function of the polar (azimuthal) angle θ_L ($\delta\phi_L$) of K_L estimated from K_S. Data (black solid dots) and MC (red open dots) are compared. The solid lines superimposed are the result of fits to the functions of equations 2 and 3.

In order to account for the data-MC difference for $\delta\theta$, we consider two possible gaussian smearing corrections: the first has a standard deviation $\sigma_\theta^{(0)}$ independent of θ_L; the other is the consequence of a data-MC difference in the reconstruction of the z coordinate of the K_L crash cluster and has a θ dependence. The effect of a gaussian correction on z

with standard deviation σ_z is indeed a θ-dependent gaussian smearing on θ:

$$\delta\theta = \frac{\delta z \sin\theta}{\rho/\sin\theta + \delta z \cos\theta}$$

The standard deviation of a gaussian smearing correction on $\delta\theta$ is therefore parametrized as follows:

$$\left\langle \delta\theta^2 \right\rangle = \left(\sigma_\theta^{(0)}\right)^2 + \left(\frac{\sin^2\theta}{\rho}\right)^2 \sigma_z^2 + \left(\frac{\sin^2\theta \sin 2\theta}{2\rho^2}\right)^2 3\sigma_z^4 \tag{2}$$

In order to account for the data-MC difference for $\delta\phi$, we consider the following parametrization for the standard deviation of a smearing correction:

$$\left\langle \delta\phi^2 \right\rangle [\mathrm{r}ad] = \sigma_\phi^{(0)} + \sigma_\phi^{(2)} \times (\phi\,[\mathrm{r}ad])^2 \tag{3}$$

The free parameters in the above formula, $\sigma_\theta^{(0)}$, σ_z, $\sigma_\phi^{(0)}$, and $\sigma_\phi^{(2)}$, are fit to the standard deviations of data and MC, as shown in the example of Fig. 4, relative to the beginning of the 2002 data taking. The fit is repeated for each of the 94 data subsets. The resulting corrections to be added in quadrature to the MC are shown in Fig. 5: each term shows no evident dependence on the data period, the constant terms are ~ 10 mrad for either $\delta\theta$ and $\delta\phi$ (to give an order of magnitude, 10 mrad is the transversal width of one calorimeter cell in the barrel), the correction on the z coordinate is $\sigma_z \sim 2$ cm, while no second order correction is needed on $\delta\phi$.

In order not to include as correction for the K_L direction $\mathbf{P}_L^{\mathrm{C}R}$ contributions from a data-MC difference on the "pointer" $\mathbf{P}_L^{\mathrm{F}S}$, we checked which are the effects on $\delta\theta$ and $\delta\phi$ of the resolutions on the K_S-pion momenta (1) and on the estimate of z_ϕ (2). For (1), we compared the results obtained by using the MC simulation with the normal track reconstruction with those obtained correcting the track momenta according to the p_t-smearing discussed in the following section and with those obtained using the true value of $\mathbf{P}_L^{\mathrm{F}S}$; for (2), we compared the results when using the estimate of z_ϕ with those for $z_\phi = 0$ and those for the true value of z_ϕ. The results from this comparisons are shown in table 5, relative to a single data subset. From the comparison of the first two set of results, we conclude that $\sigma_\theta^{(0)}$ is dominated by the resolution on the K_S-tracks: the resolution on the K_L-crash cluster accounts only for 7 mrad (last table). The result anyway is not sensitive whether the p_t-smear is applied or not. On the contrary, σ_z is not sensitive to the contribution of resolution on K_S tracks, while receives a contribution if the estimate of z_ϕ is not used: subtracting in quadrature MC results from the normal method to those with $z_\phi = 0$, this contribution is of 1.7(3) cm and it is compatible with the intrinsic variation of

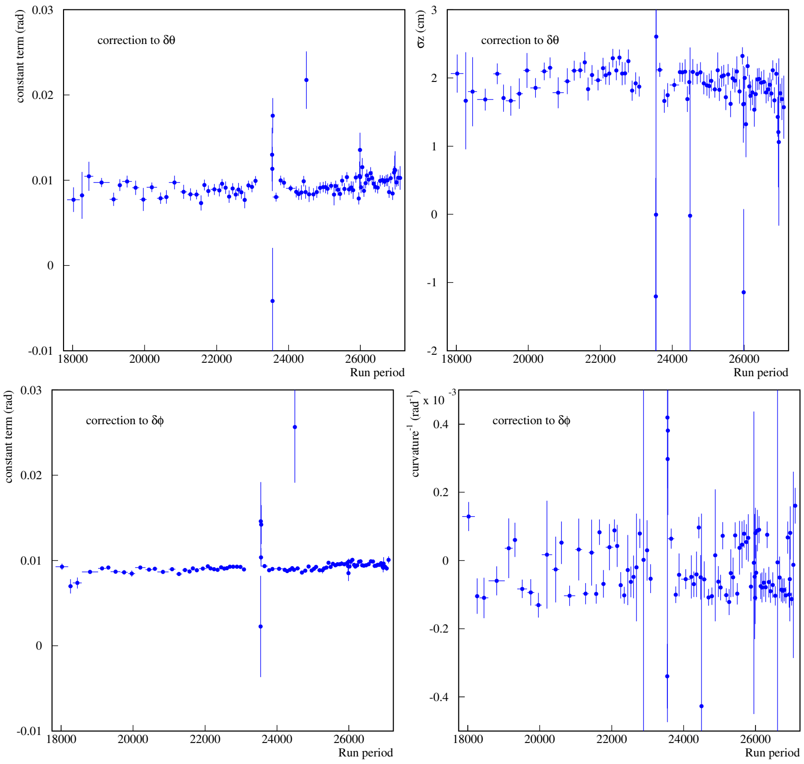

Figure 5: Parameters of a gaussian smearing correction to be applied to the $\delta\theta$ (upper panels) or $\delta\phi$ (lower panels) MC distributions. Each quantity is obtained as quadrature difference of the value for data and that for MC: if the value for MC is higher than that for data, the plotted value is negative.

Method	Source	$\sigma_\theta^{(0)}[\mathrm{m}rad]$	$\sigma_z[cm]$
Normal	DATA	25.6(2)	3.1(1)
	MC	23.7(6)	2.5(3)
	MC p_t-smear	23.8(6)	2.4(3)
$\mathbf{P}_L^{\mathrm{F}S}(true)$	MC	9.1(4)	2.60(8)
	MC p_t-smear	9.4(4)	2.54(8)
$z_\phi = 0$	DATA	24.4(3)	3.52(9)
	MC	22.8(6)	3.3(2)
	MC p_t-smear	22.7(6)	3.2(2)
$z_\phi(true)$	MC	22.1(5)	2.7(2)
	MC p_t-smear	22.2(6)	2.6(2)
$\mathbf{P}_L^{\mathrm{F}S}(true)$, $z_\phi(true)$	MC	7.0(5)	2.65(7)
	MC p_t-smear	7.1(5)	2.64(7)

Table 5: Various methods for the estimate of the corrections to the θ angle from K_L-crash are compared.

z_ϕ of 1.52(3) cm. However, comparing σ_z from the second and the fifth methods, we conclude that this contribution is completely absorbed if the z_ϕ estimate is used, thus giving robustness to the σ_z estimate. Similar conclusions are valid for the corrections to $\delta\phi$.

The corrections outlined above cure the core of the K_L-crash angular resolution. However, as explained in detail in Ref. [16, 26], the angular distribution, measured using $K_S \to \pi^+\pi^-$ events, shows both a peak and broad distribution. Using the same sample, we compared data and MC distributions, and observed a discrepancy between data and MC in the fraction of events in the broad region: the MC has more events in the peak. In order to correct for this, for 3% of the events, we add to the angle θ of the K_L-crash values sampled from a Gaussian distribution with standard deviation $\sigma(\theta) \sim 0.4°$. The effect of this correction can be seen in Fig. 6 and Fig. 7, where the distribution of the reconstructed angle between K_L and K_S for events with a K_L-crash and $K_S \to \pi^+\pi^-$ is shown, for different K_L-crash minimum energies. Without the correction, we see that the tail of the distribution in the data is higher that in the MC. This discrepancy is recovered after this smearing correction. Moreover, the same correction seems to hold for different energies of the K_L-crash. In Fig. 8 we show for the same events the distribution of the difference between the missing energy at the K_S vertex, calculated in the $\pi\pi$ mass hypothesis, and the missing momentum, $E - p$. A good agreement between data and MC is observed down to about $-20\,\mathrm{MeV}$, while an excess of events in data is still observed below this value (see the plot in logarithmic scale). The impact of this discrepancy for the reliability of the procedure used to evaluate the number of $K_S \to \pi e \nu$ events is discussed in Sec. 4.

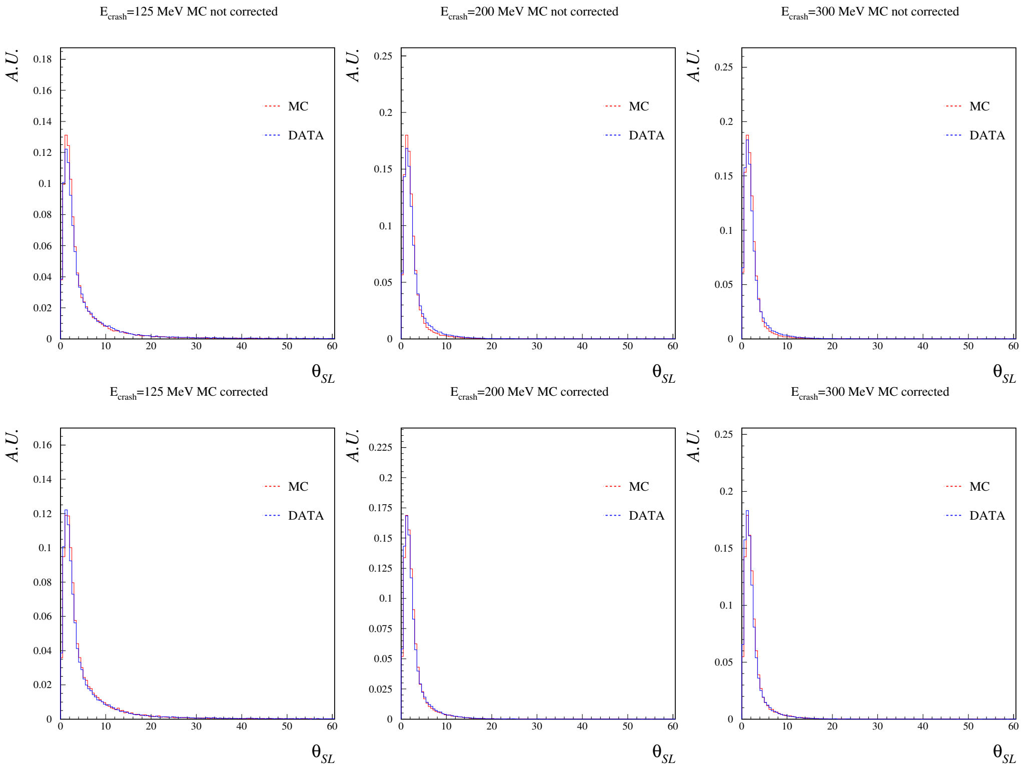

Figure 6: Distribution of the reconstructed angle between K_L and K_S for events with a K_L-crash and $K_S \to \pi^+\pi^-$, for minimum K_L-crash energies $E_{crash} = 125, 200, 300$ MeV (from left to right), for data (blue) and MC (red). The upper plot is for MC events without any correction, while the lower is for MC events with the smearing correction.

3.3 Smearing of MC resolutions for track momenta

An extensive study of the reliability of the MC in reproducing the tracking response for data has been carried on, using pion tracks from $K_S \to \pi^+\pi^-(\gamma)$ events (K_L-tag events). Three types of corrections have been implemented, in order to better the quality of the data-MC agreement.

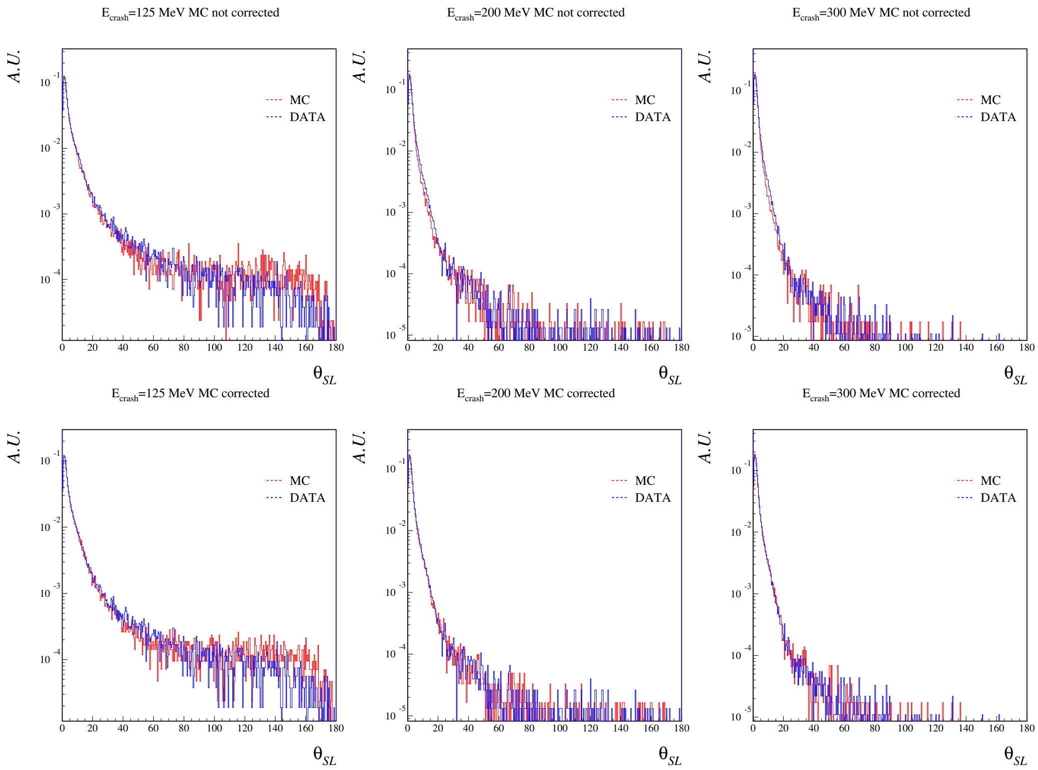

Figure 7: Distribution of the reconstructed angle between K_L and K_S for events with a K_L-crash and $K_S \to \pi^+\pi^-$, for minimum K_L-crash energies $E_{crash} = 125, 200, 300$ MeV (from left to right), for data (blue) and MC (red). The upper plot is for MC events without the smearing correction, while the lower is for events with the correction.

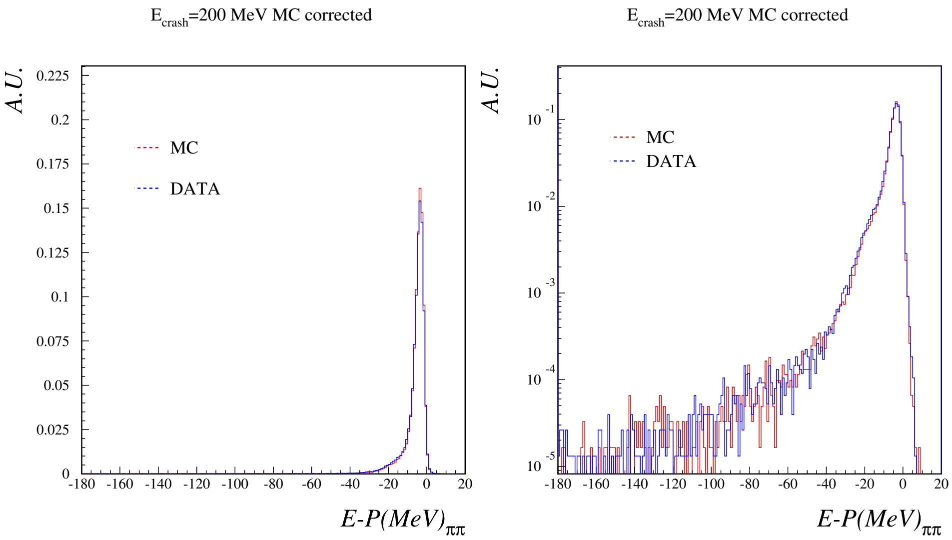

Figure 8: Distribution of the difference between missing energy in the $\pi\pi$ hypothesis and missing momentum at the K_S vertex, for events with a K_L-crash and $K_S \to \pi^+\pi^-$ decays, and minimum K_L-crash energy $E_{crash} = 200$ MeV. A good agreement is achieved between data (blue) and MC (red) after the smearing correction is applied.

We first compared distributions of the invariant mass in the π-π hypothesis for data and MC. As shown in Fig. 9, the distribution for data has a broader core than that for MC. We first addressed this problem looking at the dependency of the track momentum resolution from the s-t relation used in the reconstruction of the hit positions (for a detailed explanation of the DC calibration procedure and of the s-t relation parametrization, see [11]). We compared the track momentum resolutions obtained for different values of

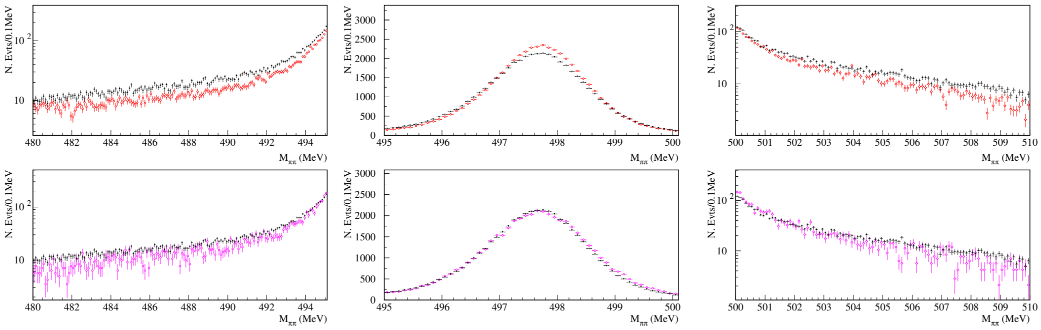

Figure 9: Distribution of 2-track invariant mass in the $\pi\pi$ hypothesis in K_L-tag events for data (black filled dots), MC (red open dots, upper panel), and MC after "p_t smearing" (purple open dots, lower panel).

the parameters describing the s-t relations. We modeled a data-MC discrepancy as arising from a time offset: we compared the reconstruction outputs obtained from the s-t relation obtained by calibrating the MC simulation as done for data with that obtained after calibrating in presence of a time offset. The effect of a time offset is a worsening of the momentum resolution with a standard deviation proportional to the transverse momentum ("p_t smearing"):

$$\sigma_P = \sigma^{(0)} + \sigma^{(1)} P_t$$

The values of the smearing correction for the track momenta have been determined by minimizing the difference between core widths for the data and MC; we obtain $\sigma^{(0)} = -0.09$ MeV and $\sigma^{(1)} = 0.0016$.

The data-MC discrepancy shown in Fig. 9 is partly recovered in the region of the left and right $M_{\pi\pi}$ tails, too. Left and right tails are populated by tails of the tracking resolution, while the left tail also receives contribution from $\pi\pi\gamma$ events with hard radiation and by events with early $\pi \to \mu\nu$ decays. It is fundamental to have a good understanding of the left tail, since the events with $M_{\pi\pi} < 480$ MeV are the potential background for the K_{e3} selection. Therefore, in order to study the far tail of the single-track resolution, a dedicated analysis has been built.

Quantity	Data	MC	Pointer$-$MC	particle
Mean, $\|\mathbf{P}^*\|[MeV]$	206.02(4)	205.94(3)	-0.005(30)	π^+
Mean, $\|\mathbf{P}^*\|[MeV]$	205.98(4)	205.98(3)	-0.056(31)	π^-
Resolution, $\|\mathbf{P}^*\|[MeV]$	0.99(4)	0.94(3)	0.81(2)	π^+
Resolution, $\|\mathbf{P}^*\|[MeV]$	0.98(4)	0.99(3)	0.81(3)	π^-
Mean, $\delta\theta[^\circ]$			-0.04(2)	π^+
Mean, $\delta\theta[^\circ]$			-0.04(2)	π^-
Resolution, $\delta\theta[^\circ]$			0.47(2)	π^+
Resolution, $\delta\theta[^\circ]$			0.49(2)	π^-

Table 6: Data-MC comparison of the track momentum boosted in the K_S rest frame. In the "Pointer$-$MC" column we show the difference between the value calculated from the kinematic closure and the true MC value.

The K_L is required to decay far from the origin ($\rho > 110$ cm) into K_{e3} or $K_{\mu3}$, by applying kinematic and TOF cuts. The kinematics is then closed at the K_S vertex using the K_L momentum from the direction of the K_L vertex and only one K_S track, whose momentum is extrapolated backward to the point of closest approach to the K_S line of flight known from the K_L, and then boosted in the K_S frame ($\mathbf{P}^*$).

There is a very good data-MC agreement for the values of mean and standard deviation of the $\mathbf{P}^*$ distribution, as shown in table 6. The momentum of the other track is then estimated closing the kinematics. The "pointer" is compared with the MC truth: mean and standard deviation are calculated for the residual of the modulus and of the θ angle. As shown in table 6, the mean of the estimate from the pointer is compatible within the error with the true value, while 800 keV and $\sim 0.5^\circ$ are the resolutions for the pointer modulus and θ angle, respectively.

The momentum $|\mathbf{P}^*|$ in the K_S frame is required to be around the monochromatic value $\sqrt{m_k^2 - m_\pi^2/4} \sim 206$ MeV. The tracking resolution is then calculated as the difference between the momentum of the other track and the estimated momentum (pointer). Resolution functions for the modulus, the θ angle, and the ϕ angle are considered, in 40 MeV $\times$ 20 MeV bins of longitudinal vs transverse momentum, p_z vs p_t. Examples of these resolution plots for the modulus are shown in figure Fig. 10. Data and MC momentum-resolution distributions are compared. The fraction of events in the "core" ($[-8, +8]$ MeV) and in the left ($[-30, -8]$ MeV) and right ($[+8, +20]$ MeV) tails are used to determine the fit function: if the "core" fraction is above (below) 94%, we fit the resolution to the sum of two (three) gaussians, as shown in Fig. 10. The standard deviation of the more populated gaussian is shown in Fig. 11 for data and MC; the quadrature

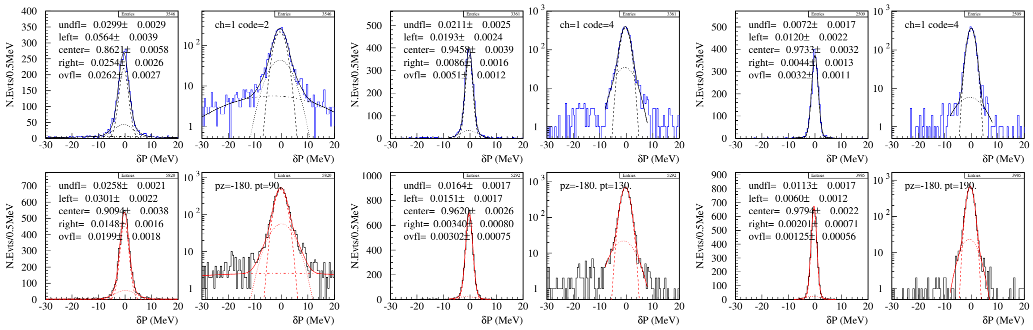

Figure 10: Momentum resolution for π^+ tracks for data (upper panels) and MC (lower panels). Different values of p_t are shown for the same p_z bin. For each plot, shown either in logarithmic (right panels) and in linear (left panels) scale, the fraction of events in the regions $[-\inf, -8]$ MeV (undfl), $[-30, -8]$ MeV (left),$[-8, +8]$ MeV (central),$[+8, +20]$ MeV (right),$[+20, +\inf]$ MeV (ovfl), are also shown. The results from fits to the sum of three (code=2) or two (code=4) gaussians are shown.

difference between data and MC is also shown. This correction confirms what has been estimated looking at the invariant mass: there is a positive p_t dependence of the quadrature difference, which is of the order of 0.3-0.4 MeV. It is also evident that one should better parametrize it in terms of p_t and p_z (or θ). We decided to directly take the average value of this quadrature difference for each p_t-p_z bin, extrapolating to the bins not populated by the tagged tracks, if necessary.

Besides the correction for the resolution core we observed that the number of events in the tails is underestimated by the MC, with respect to data. The data-MC difference between the fraction of events in the cited regions is shown in Fig. 12. The $\sim 1\%$ difference translates into a 50% underestimation relative to the amount of events in the tails. In order to correct for this, we design a procedure that randomly downscales a MC event if the difference between reconstructed and true momentum lies in the central region. The effectiveness of this procedure has been proven on the same sample of $K_S \to \pi^+\pi^-(\gamma)$, $K_L \to K_{l3}$ decays. However, the effect on the simulation of the background for the K_{Se3} selection turned out to be negligible [2].

[2]A tentative interpretation for this is that, despite our efforts, the correlations between the various parameters of a badly reconstructed track (modulus, polar and azimuthal angles of the momentum) are still not correctly simulated.

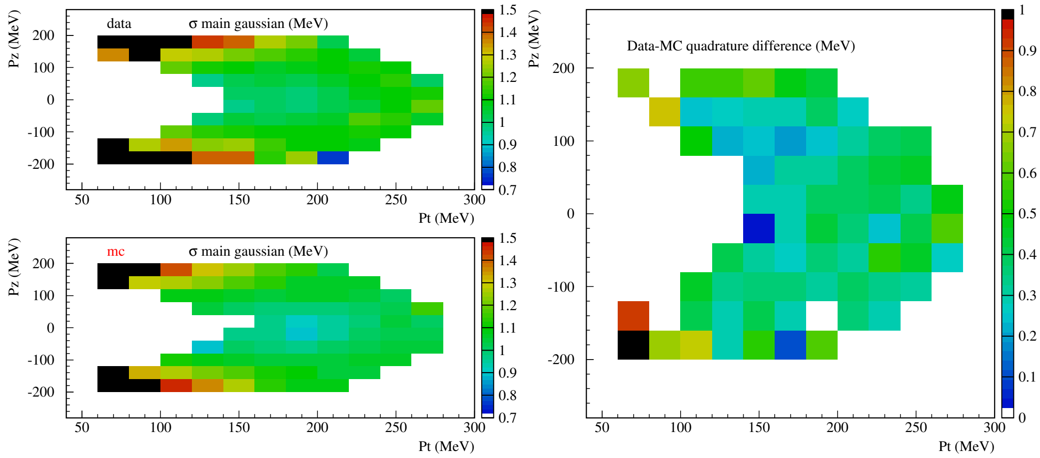

Figure 11: Standard deviation of the main gaussian for π^+ tracks for data (left upper) and MC (left lower), as a function of the longitudinal and transverse momentum p_z and p_t. The quadrature difference between data and MC is also shown (right panel).

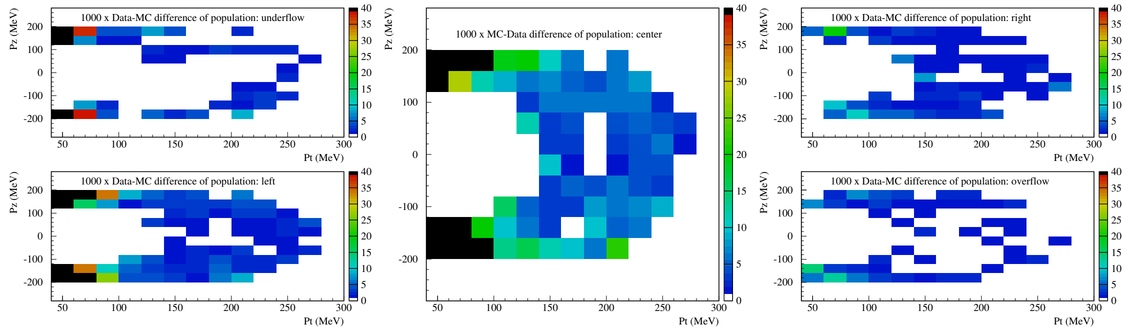

Figure 12: Difference between MC and data of the fraction of events in various regions of the momentum resolution, for π^+ tracks: underflow ($\delta P \in [-\inf, -30]$ MeV) and left ($\delta P \in [-30, -8]$ MeV) (left panels); central ($\delta P \in [-8, +8]$ MeV) (central panel); right ($\delta P \in [+8, +20]$ MeV) and overflow ($\delta P \in [+20, +\inf]$ MeV) (right panels).

3.4 Smearing of MC resolutions for cluster times

Since the signal selection is based on a Tof technique, we tried to improve the resolution of the time measurement and to reduce the disagreement of the time response of the calorimeter between data and MC. In order to improve the Tof resolution, we subtracted from the measured time in the calorimeter the average time needed by the particle to travel from the impact point on the calorimeter to the cluster centroid. In fact, this lapse of time is of the order of 100 ps, *i.e.* of the order of the cluster time resolution (~ 200 ps) and it depends on the particle type and momenta. Therefore, the Tof resolution improves taking into account the small piece of path between the particle impact point on the calorimeter, and the centroid position (the so called "pezzetto"). This correction is separately evaluated and applied to data and MC, thus improving the agreement between the simulation and the data. In the next section we describe how we measured from the Tof correction, and how it is applied to data and MC. In Sec. 3.4.2 we discuss the differences observed in the time resolution between data and MC and the correction applied to the MC.

3.4.1 "Pezzetto" and "Datizza"

For the implementation of the single-particle method we have tagged several kind of particles from different control samples: Electrons from Bhabha and $K_L \to \pi e \nu$ events; Pions from $K_S \to \pi^+\pi^-$ and $\phi \to \pi^+\pi^-\pi^0$ decays; Muons from pion decays. For each of these particles, we calculate the point and the direction of impact on the calorimeter surface, extrapolating from the track end. Clusters closer than 1 m to the impact point are considered. The distance between the impact point and the cluster centroid position is projected on the direction of impact ($d_{\rm long}$) and on the direction normal to it ($d_{\rm tra}$). Clusters with $d_{\rm tra} < 30$ cm are associated to the track.

The distribution of the average difference δ_t between the cluster time and the expected time of flight at the calorimeter surface as a function of $d_{\rm long}$ is parametrized as a straight line, $a + b \times d_{tra}$. The a and b parameters are obtained for different values of the particle momentum and treating separately the cases in which the particle reaches the barrel or the endcap. The dependence of the parameters $a(p)$ and $b(p)$ on the momentum p is shown in Fig. 13, for positive and negative pions with impact on the barrel.

Two different approaches are used for data and MC. For data events, a linear parametrization of the momentum dependence of data $a(p)$ and $b(p)$, is used to correct the expected time of flight of the particles ("Pezzetto" correction), before the signal selection. For MC events, we first reproduce the data behavior of the parameters $a(p)$ and $b(p)$: the difference of data and MC parameters is parametrized as a cubic polynomial and it is used to correct the time of flight of the particles ("Datizza" procedure). Then, the MC is treated

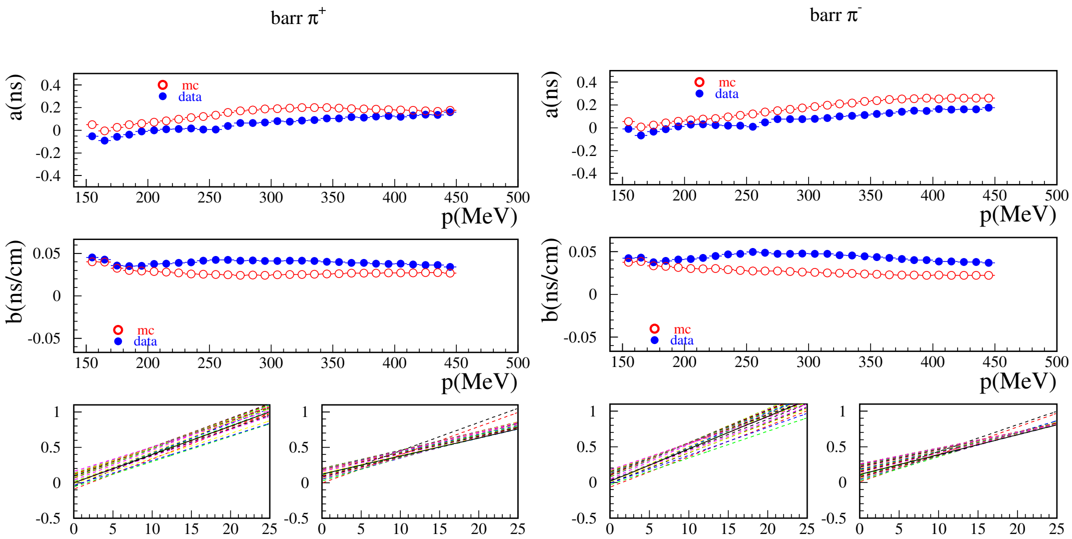

Figure 13: Parameters a and b as a function of the particle momentum, for positive (left) and negative (right) pions, with impact on the barrel. Both data (blue) and MC (red) are shown. The lower plots show the parametrizations of δ_t in ns, as a function of the distance d_{long} in cm for data (left panels) and MC (right panels).

as the data, and the same pezzetto-correction is applied.

3.4.2 The "Smirizza" procedure

Using the same single-particle samples, we measured the standard deviation of δ_t. This is shown in Fig. 14 for pions, as a function of the particle momentum.

When analyzing a MC event, we would correct the cluster time associated to each charged particle adding a time sampled from a Gaussian distribution with standard deviation equal to the difference in quadrature of data and MC resolutions (if it is greater than zero).

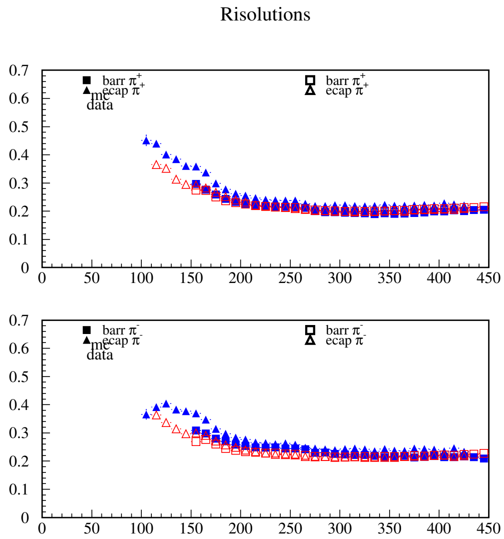

Figure 14: Time resolution, expressed in ns, measured for pions, as a function of the momentum in MeV. The upper plot is for positive pions, while the lower in for negative pions. Data is shown in blue while MC is in red. Points referring to particles with impact on barrel (endcap) are shown with a squares (triangles).

However, this procedure doesn't fix correctly the time resolution. In fact, there are three terms entering in the time resolution. This can be expressed as a function of the energy as:

$$\sigma_{\delta_t} = \frac{a(ps)}{\sqrt{E(\mathrm{GeV})}} \oplus b(ps) \oplus c(ps), \tag{4}$$

where $a(ps)$ is the stochastic term, $b(ps)$ is the uncorrelated constant term, and $c(ps)$ is the correlated constant term. Then, while a and b are always present in a time measurement,

c is equal for all the cluster in an event, and cancels out in the difference. Indeed, the resolution for time differences is:

$$\sigma_{\Delta(\delta_t)} = \frac{a(ps)}{\sqrt{E^*(\text{GeV})}} \oplus \sqrt{2}b(ps),$$

where

$$E^* = \frac{E_1 E_2}{E_1 + E_2}, \tag{5}$$

and $E_{1,2}$ are the cluster energies. Therefore, if b and c are different in data and MC, two different corrections must be applied if a cut is applied to absolute times, or to their differences.

The three parameters entering in Eq. (4) and Eq. (5), are obtained using photons from $\phi \to \pi^+\pi^-\pi^0$. $\phi \to \pi^+\pi^-\pi^0$ are selected by cutting on the missing mass, by cutting on the angle between the two photons in the ϕ rest frame, and by a loose cut on the photon beta. For each event, we calculate $T - R/c$ and $\Delta(T - R/c)$, distinguishing between events in the barrel-barrel, barrel-endcap, and endcap-endcap configuration. The dependence of these two quantities on the energy E and E^*, respectively, is fit to the function $P1(ps)/\sqrt{E(GeV)} \oplus P2(ps)$, as shown in Fig. 15. Form the fit results, and using Eq. (4) and Eq. (5), we extract the parameters a, b, and c. The results for barrel, for both data and MC, as a function of the data period, are shown in Fig. 16.

The average values for data are:

$$\sigma_{t,barrel} = \frac{57.1(1)\text{ ps}}{\sqrt{E(\text{GeV})}} \oplus 105(1)\text{ ps} \oplus 92(1)\text{ ps}, \tag{6}$$

$$\sigma_{t,endcap} = \frac{62.5(2)\text{ ps}}{\sqrt{E(\text{GeV})}} \oplus 120(2)\text{ ps} \oplus 116(3)\text{ ps}, \tag{7}$$

and for MC:

$$\sigma_{t,barrel} = \frac{61.6(1)\text{ ps}}{\sqrt{E(\text{GeV})}} \oplus 1(2)\text{ ps} \oplus 127.8(3)\text{ ps}, \tag{8}$$

$$\sigma_{t,endcap} = \frac{62.9(2)\text{ ps}}{\sqrt{E(\text{GeV})}} \oplus 13(3)\text{ ps} \oplus 122.1(6)\text{ ps}, \tag{9}$$

where the error is statistical only. While the uncorrelated term is different from zero for the data (105 and 120 ps for barrel and endcap), it is compatible with zero or negligible in the MC. Then, when computing time differences in the MC, the standard deviation is underestimated. Therefore, each time we compute a time difference in the MC, we add a further term extracted randomly from a Gaussian, with standard deviation equal to 120 ps, both for barrel and endcap.

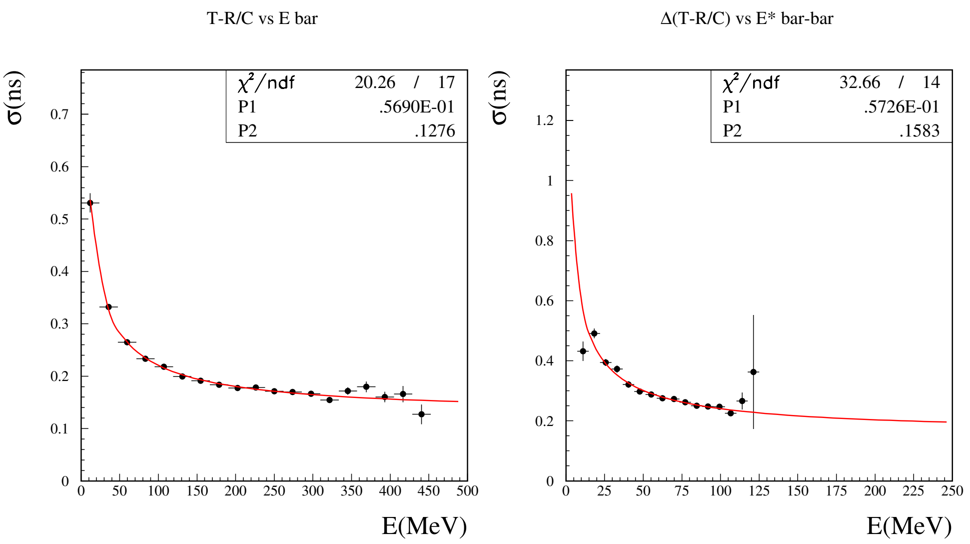

Figure 15: Left: Resolution of $T - R/c$ as a function of the cluster energy E, for events with the photon on the barrel. Right: Resolution of $\Delta(T - R/c)$ as a function of the average energy $E_1E_2/(E_1 + E_2)$.

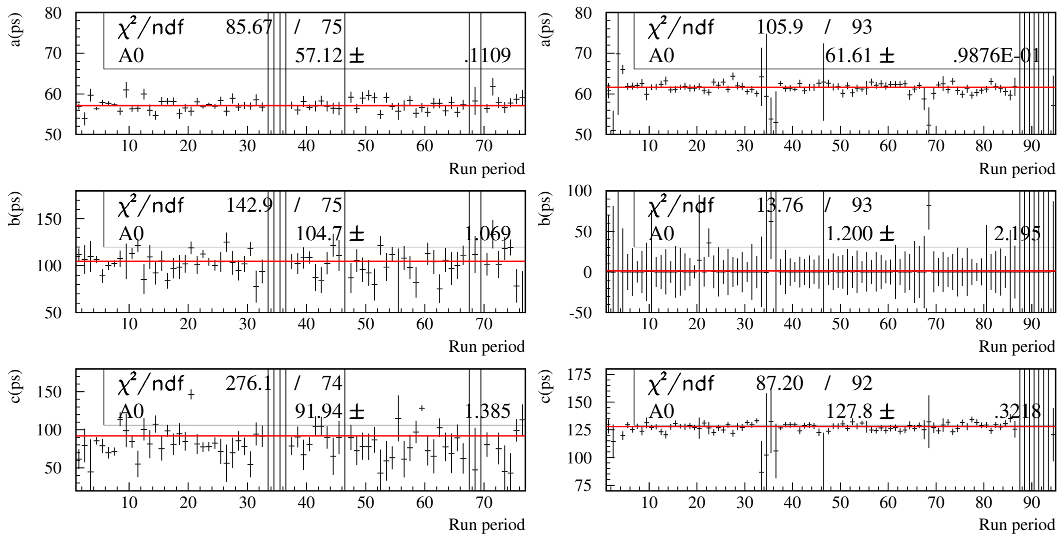

Figure 16: Values of the three parameters a, b, and c for barrel, as a function of the data period, for data (Left) and MC (Right). A linear fit is superimposed.

3.5 Tof and trigger-sector efficiencies and T_0 distribution

We measure many efficiencies, such as TRK, T_0, TCA, and sector efficiency from data using two different methods: the single-particle and the double-particle method. On the contrary, we measure the efficiency for Tof and the T_0 population from the control sample of $K_L \to \pi e \nu$ decays before the DC. In the single-particle method the efficiencies are measured as a function of kinematic variables, such as P_t and P_Z, and are then weighted using the MC kinematic for signal events. In this way, no bias is introduced by the selection in the kinematic distributions, and the efficiencies are weighted correctly. The same is not true for the $K_L \to \pi e \nu$ sample. In fact, it requires a different selection with respect to the signal, has decays up to 25 cm from IP , and is tagged with $K_S \to \pi^+\pi^-$ events. All these differences change the kinematic distribution of the decay, and in particular, the fraction of events in which a pion or an electron reaches the barrel or the end-caps. These effects, which were neglected in the past (mainly for lack of time), are however very important. This is shown in Tab. 7, where the efficiencies measured for the three different Tof cuts are shown for the $K_L \to \pi e \nu$ sample, data and MC, and the MC signal. The last row shows the combined efficiencies:

$$\epsilon_{combined} = \epsilon_{KLdata} \times \frac{\epsilon_{KSMC}}{\epsilon_{KLMC}}. \tag{10}$$

In the old analysis, we used the efficiencies $\epsilon(\Delta\delta T_{\pi\pi})$ and $\epsilon(\Delta\delta T_{\pi e})$ shown in the first row (data K_{Le3}), while a more precise estimate is given by the last row (Combined). Comparing the two rows, we observe that while $\epsilon(\Delta\delta T_{\pi e})$ is practically unchanged, $\epsilon(\Delta\delta T_{\pi\pi})$ changes by about 3% [3]. This is explained by the fact that since the variable $\Delta\delta T_{\pi e}$ is calculated using the correct mass assumption, it is centered at zero, and the effect of the different kinematic distribution of the sample is only a slight change in the resolution. On the contrary, the $\Delta\delta T_{\pi\pi}$ distribution is calculated using a wrong mass assumption, so that it is not centered to any fixed value, and the shape of the distribution depends on the kinematic of the decay.

The estimated efficiency $\epsilon_{combined}$ is exact if the two sample efficiencies, ϵ_{KLdata} and ϵ_{KLMC}, or the two MC efficiencies, ϵ_{KLMC} and ϵ_{KSMC}, are equal. In fact, given three efficiencies ϵ_a, ϵ_b, and ϵ_c, we could in principle correct the inefficiency $(1-\epsilon)$:

$$\overline{(1-\epsilon)} = (1-\epsilon_a) \times \frac{(1-\epsilon_b)}{(1-\epsilon_c)},$$

instead of the efficiency:

$$\overline{\epsilon} = \epsilon_a \times \frac{\epsilon_b}{\epsilon_c}.$$

[3]This effect might be smaller with the old analysis where the cut is $|d\delta_{t,\pi\pi}| > 1.4$ ns.

Source	$\epsilon(\Delta\delta T_{\pi\pi})$	$\epsilon(\Delta\delta T_{\pi e})$	$\epsilon(\delta T_{\pi}$ vs $\delta T_e)$
DATA K_{Le3}	88.7(1)	94.0(1)	90.7(1)
MC K_{Le3}	87.6(1)	93.50(8)	92.35(9)
MC K_{Se3}	90.61(6)	93.69(5)	93.50(5)
Combined	91.5(1)	94.2(1)	92.03(2)

Table 7: Tof efficiencies for data and MC control samples and for MC signal. The control samples efficiencies are obtained without weighting the P_T distributions and selecting $\rho_{vtx} < 25$ cm. The second error within parentheses in the last line are systematic (Eq. 11).

Source	$\epsilon(\Delta\delta T_{\pi\pi})$	$\epsilon(\Delta\delta T_{\pi e})$	$\epsilon(\delta T_{\pi}$ vs $\delta T_e)$
DATA K_{Le3}	90.4(3)	94.6(2)	91.5(3)
MC K_{Le3}	89.6(2)	94.0(2)	93.7(2)
MC K_{Se3}	90.61(6)	93.69(5)	93.50(5)
Combined	91.3(3)	94.3(3)	91.3(4)

Table 8: Tof efficiencies for data and MC control samples and for MC signal. The control samples efficiencies are obtained without weighting the P_T distributions and selecting $\rho_{vtx} < 10$ cm.

However, the sum of the two is not equal to one:

$$\overline{\epsilon} + \overline{(1-\epsilon)} = 1 + \frac{(\epsilon_c - \epsilon_b)(\epsilon_c - \epsilon_a)}{\epsilon_c(1-\epsilon_c)}. \tag{11}$$

The extra term in the right-hand side of Eq. 11 gives a systematic uncertainty in the efficiency determination. Comparing the numbers in Tab. 7, we see that the systematic error is expected to be small. However, we tried to improve the agreement between the control sample and the signal by selecting only the K_L with a vertex transverse distance $\rho_{vtx} < 10$ cm. The results for the efficiencies are shown in Tab. 8. As expected, the agreement between the efficiencies of MC sample and MC signal increases, and so the combined efficiencies with the data-sample efficiencies.

To further improve this agreement, we compared the kinematic distributions of the control samples with that of the MC signal, and observed that the main difference lies in the transverse momentum distributions, and in the fraction of events with the electron, the pion, or both the particles associated to a cluster in the barrel. Therefore, we weight each event, of both data and MC control samples, for the ratio of $(P_{t,\pi}, P_{t,e})$ distributions of samples and signal. We made a weight distribution for each configuration of association of the particles: barrel-barrel, barrel-endcap, endcap-barrel, and endcap-endcap. The normalization of the weights is such that the relative difference between association-configurations is also corrected: The samples have higher fraction of events with both pion and electron associated to clusters on the barrel, and so the barrel-barrel configuration has a smaller average weight. Examples of such weight-distributions are shown in Fig. 17 and Fig. 18. The effect of the weights on the P_Z and P_t distributions for electron on the endcap is shown in Fig. 19 and Fig. 20, respectively.

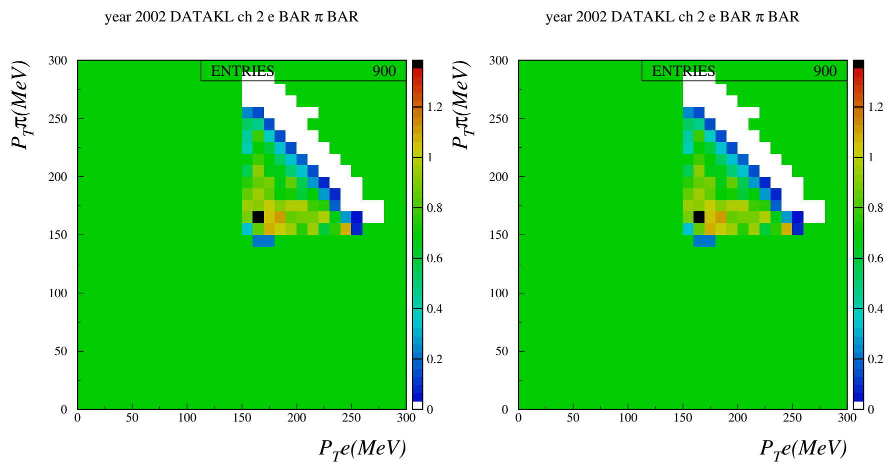

Figure 17: Left: Weight distribution for the barrel-barrel configuration, for $K_L \rightarrow e^-\pi^+\overline{\nu}$ data events. Right: The same for the MC sample. The white bands, corresponding to values of the weights close to zero, show that, because of the different selection, the P_t distribution of the signal is softer than the sample one.

The Tof efficiency is shown in Fig 21 as a function of the electron P_t before and after the weighting procedure. Comparing it with the P_t distribution in Fig. 20, we see that the difference in the total efficiencies arises from the different kinematic of the decays.

Finally, the distributions of the Tof variables used for the selection are shown in Fig. 22 and Fig. 23.

The efficiencies obtained with the corrected samples are shown in Tab. 9 [4]. We observe a nice agreement between the two MC efficiency, and therefore, between the data sample

[4]The careful reader will notice that the efficiencies for K_{Se3} MC are slightly different from those in Tab. 7 and 8. The small effect is due to the presence of overflow events in our efficiency histograms, that were not taken into account in the previous tables. However this effect is well within the statistical error.

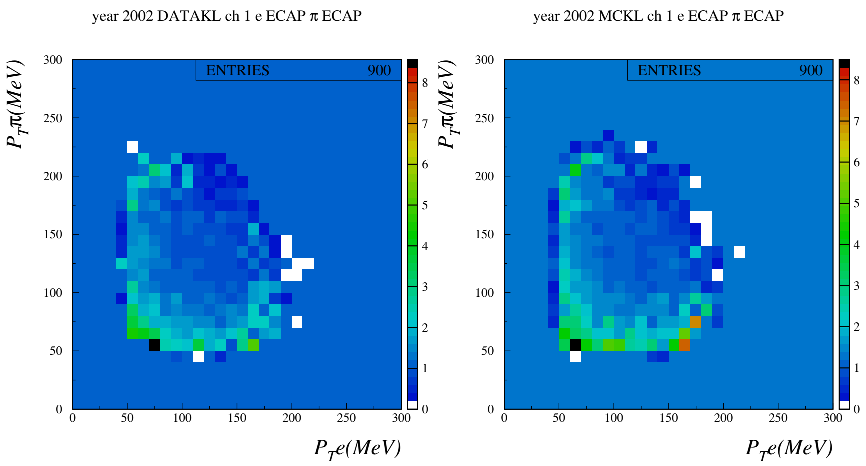

Figure 18: Left: Weight distribution for the endcap-endcap configuration, for $K_L \to e^+\pi^-\nu$ data events. Right: The same for the MC sample.

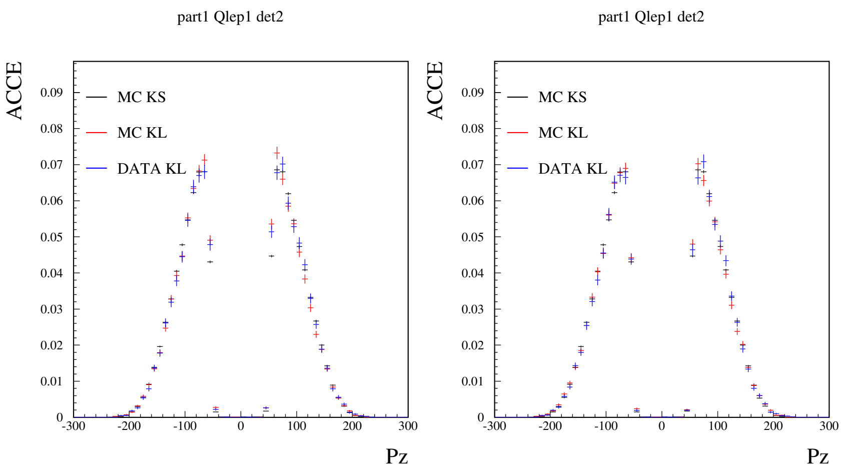

Figure 19: Left: Unweighted electron P_Z distribution for e^+ in the endcap. Right: Same distribution as before, but after the weight has been applied. MC signal is in black, MC sample is in red, and data sample is in blue.

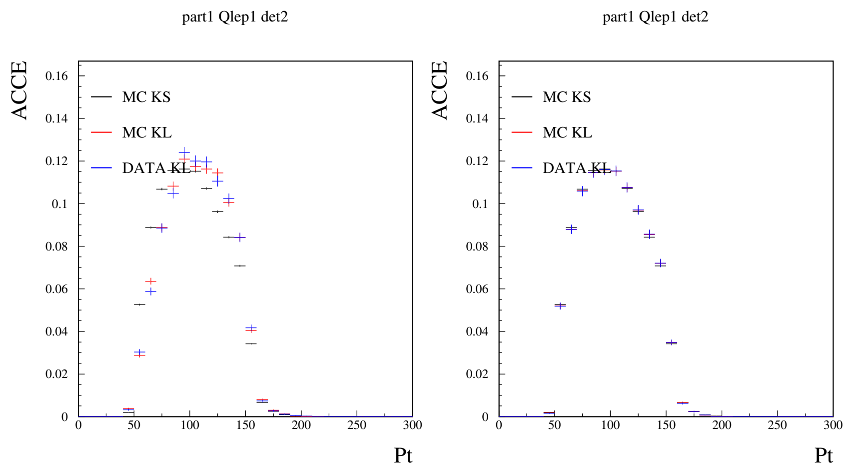

Figure 20: Left: Unweighted electron P_t distribution for e^+ in the endcap. Right: Same distribution as before, but after the weight has been applied. MC signal is in black, MC sample is in red, and data sample is in blue.

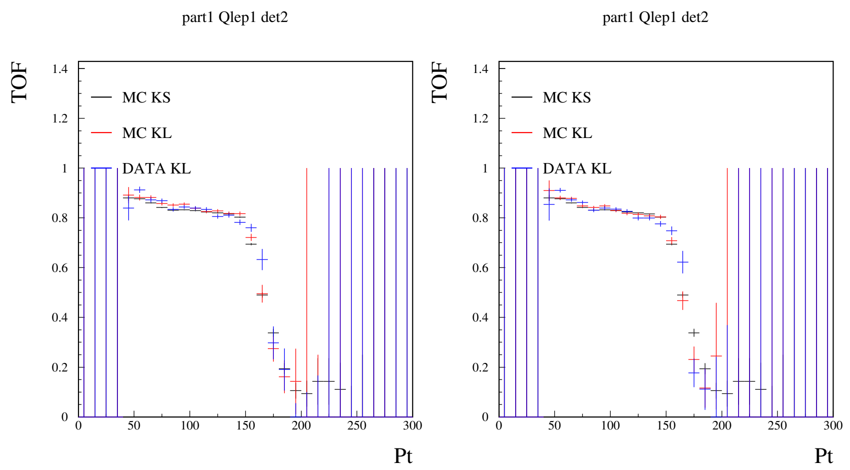

Figure 21: Left: Tof efficiency as a function of electron P_t for e^+ in the endcap, without weighting the sample events. Right: Same as before but using the weights. MC signal is in black, MC sample is in red, and data sample is in blue.

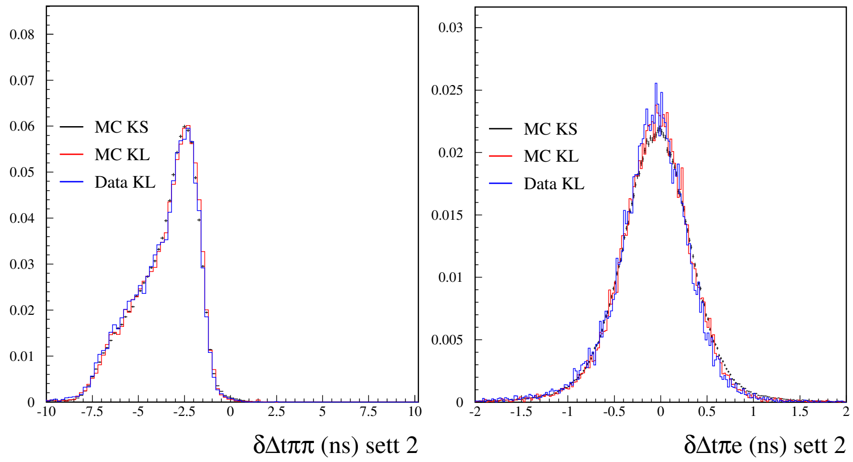

Figure 22: Left: $\Delta\delta T_{\pi\pi}$ distribution for $e^{-}\pi^{+}$ events. Right: $\Delta\delta T_{\pi e}$ distribution for $e^{-}\pi^{+}$ events. The distributions for the control samples are obtained after the weight correction. MC signal is in black, MC sample is in red, and data sample is in blue.

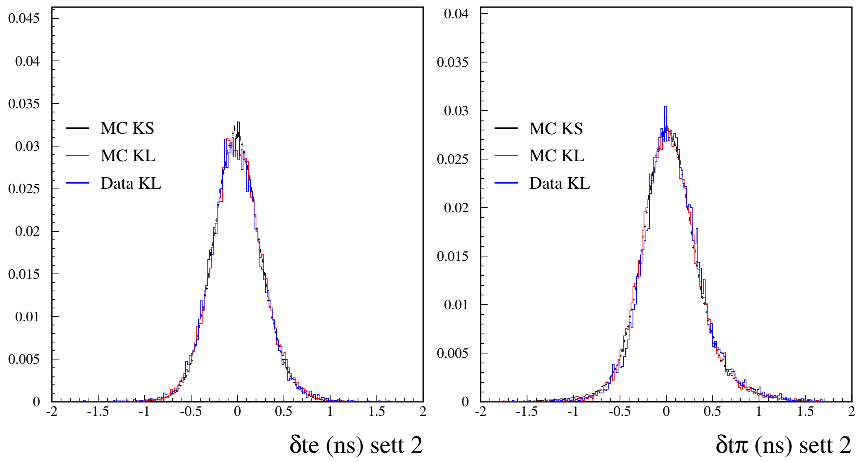

Figure 23: Left: δT_{e} distribution for $e^{+}\pi^{-}$ events. Right: δT_{π} distribution for $e^{-}\pi^{+}$ events. The distributions for the control samples are obtained after the weight correction. MC signal is in black, MC sample is in red, and data sample is in blue.

Source	$\epsilon(\Delta\delta T_{\pi\pi})$	$\epsilon(\Delta\delta T_{\pi e})$	$\epsilon(\delta T_\pi$ vs $\delta T_e)$
DATA K_{Le3}	91.3(3)	94.5(2)	91.7(3)
MC K_{Le3}	90.8(2)	93.9(2)	93.4(2)
MC K_{Se3}	90.77(6)	93.66(5)	93.44(5)
Combined	91.3(3)	94.3(3)	91.8(4)

Table 9: Tof efficiencies for data and MC control samples and for MC signal. The control samples efficiencies are obtained weighting the P_T distributions and selecting $\rho_{vtx} < 10$ cm.

efficiencies and the combined one. The differences between the combined efficiencies, estimated with the three different methods, are small and within the errors shown in the last table. However, we will use the efficiencies estimated with the weighted samples, even if they have bigger statistical error than those in Tab. 7. We will therefore consider the statistical errors as inclusive of the systematic one.

After the estimate of the Tof efficiencies, we used the weighted samples to estimate the trigger sector efficiencies and the T_0 distribution. The comparison for data and MC sample and MC signal are shown in Fig. 24 and Fig. 25.

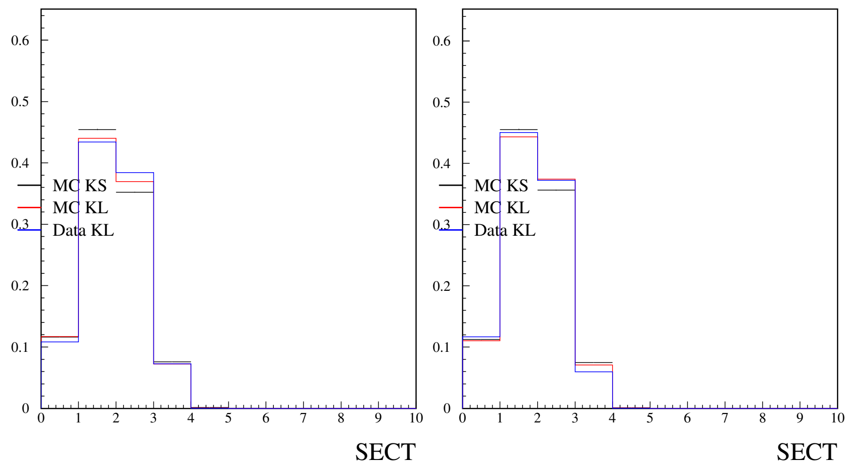

Figure 24: Left: Trigger sector efficiency for $e^+\pi^-$ events. Right: Trigger sector efficiency for $e^-\pi^+$ events. The distributions for the control samples are obtained after the weight correction. MC signal is in black, MC sample is in red, and data sample is in blue.

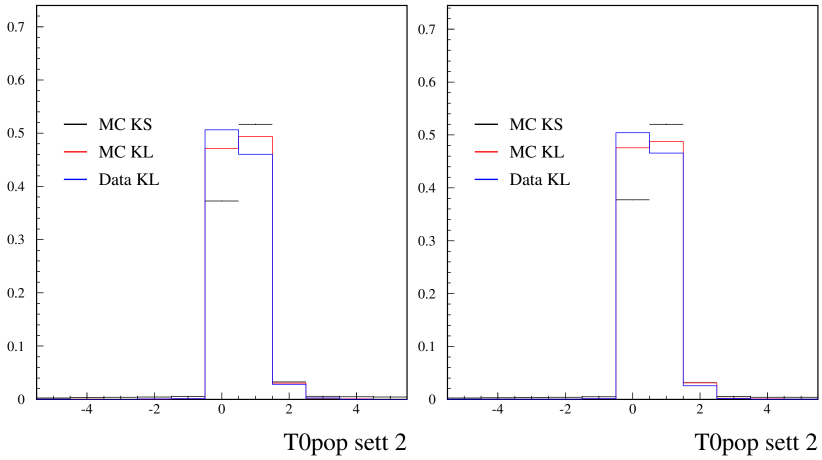

Figure 25: Left: T_0 distribution for $e^+\pi^-$ events. Left: T_0 distribution for $e^-\pi^+$ events. The distributions for the control samples are obtained after the weight correction. MC signal is in black, MC sample is in red, and data sample is in blue.

3.6 Cosmic Veto efficiency

The cosmic veto efficiency is usually determined from downscaled events, by simply counting the fraction of events that are rejected by the filter. The cosmic veto (CV) (in)efficiency is given by:

$$P(CV) = \frac{N2/p}{N1 + N2/p}, \tag{12}$$

where $N1$ is the number of events that survive the CV filter and $N2$ are the vetoed events downscaled with frequency p. The error on the efficiency is given by:

$$\sigma_{CV}^2 = \frac{N1N2(N1+N2)p^2}{(N2+N1p)^4}$$

For the data collected in the year 2001 $p = 0.2$. For ~ 2000 K_{Se3} selected per charge and a CV efficiency $\sim 4\%$, we have $\sigma_{CV} = 0.9\%$, giving a contribution of $\sim 0.9\%$ to the final error. This error can be reduced by observing that in events tagged with a K_L-crash, the probability to fire at least two CV sectors is given by:

$$P(CV)_i = P(\geq 2)_{cr} + P(1)_{cr} \times P(>0)_i + P(0)_{cr} \times P(\geq 2)_i,$$

where $P(\geq 2)_{cr}$ ($P(\geq 2)_i$) is the probability for the K_L-crash ($K_S \to i$) to fire at least two sectors, $P(1)_{cr}$ the probability for the K_L-crash to fire one sector, and $P(>0)_i$ the probability for the K_S to fire at least one sector. We define the fraction of events where the K_L-crash fires at least two CV sectors as:

$$f(2)_i = \frac{P(\geq 2)_{cr}}{P(\geq 2)_{cr} + P(1)_{cr} \times P(>0)_i + P(0)_{cr} \times P(\geq 2)_i}.$$

Since $P(\geq 2)_{cr}$ is independent of the K_S decay channel (neglecting small effects due to the T_0 populations), the ratio of the CV probabilities for the two channels $\pi\pi$ and $\pi e\nu$ is given by:

$$\frac{P(CV)_{\pi\pi}}{P(CV)_{\pi e\nu}} = \frac{f(2)_{\pi e\nu}}{f(2)_{\pi\pi}}.$$

Therefore, the correction to the ratio of branching ratio is:

$$\frac{1 - P(CV, \pi\pi)}{1 - P(CV, \pi e\nu)} = \frac{1 - P(CV, \pi\pi)}{1 - P(CV, \pi\pi) f(2)_{\pi\pi}/f(2)_{\pi e\nu}}. \tag{13}$$

$P(CV, \pi\pi)$ and $f(2)_{\pi\pi}$ are measured with high precision from downscaled $\pi^+\pi^-$ events. For $E_{\text{cr}} = 200$ MeV in the year 2001 we have:

$$\begin{aligned} P(CV, \pi\pi) &= (4.354 \pm 0.012)\% \\ f(2)_{\pi\pi} &= (69.37 \pm 0.17)\%. \end{aligned} \tag{14}$$

$f(2)_{\pi e\nu}$ is instead evaluated with about 10% accuracy:

$$\begin{aligned} f(2)_{\pi^- e^+ \nu} &= (74 \pm 10)\%, \\ f(2)_{\pi^+ e^- \overline{\nu}} &= (91.7 \pm 8.0)\%. \end{aligned} \tag{15}$$

The corrections in Eq. 13 are given by:

$$\frac{1 - P(CV, \pi\pi)}{1 - P(CV, \pi^- e^+ \nu)} = 0.9942 \pm 0.0058, \tag{16}$$

$$\frac{1 - P(CV, \pi\pi)}{1 - P(CV, \pi^+ e^- \overline{\nu})} = 0.989 \pm 0.0029. \tag{17}$$

Following the method from Eq. (12), we obtain:

$$\begin{aligned} \frac{1 - P(CV, \pi\pi)}{1 - P(CV, \pi^- e^+ \nu)} &= 0.9962 \pm 0.0092, \\ \frac{1 - P(CV, \pi\pi)}{1 - P(CV, \pi^+ e^- \overline{\nu})} &= 0.9802 \pm 0.0069, \end{aligned} \tag{18}$$

which is in agreement with our previous estimate, but has a relative error worse by a factor of ~ 2.

4 Event counting: new fit procedure

The MC description of the background distributions is not satisfactory. This imposed to obtain a deeper understanding of the various background topologies, as explained in the following section. Different mechanisms can lead a $K_S \to \pi^+\pi^-(\gamma)$ event to satisfy the selection criteria: one or both tracks can be badly reconstructed, shifting both the invariant mass and the ToF variables, or one or both associated clusters can be reconstructed with time lying in the tail of the resolution; one pion can decay to a muon before reaching the tracking volume, so that the vertex is reconstructed from the pion and muon tracks; finally, the emitted photon radiated at the K_S vertex can be "hard", $E*_\gamma > 7\,\mathrm{MeV}$, so that the invariant mass lies in the region $M_{\pi\pi} < 490\,\mathrm{MeV}$ and the contribution of the tails of the time-response is enhanced.

Our experience taught us that the MC is not reliable in reproducing these tails since, despite our efforts [27], nuclear interactions of low-momentum pions are not correctly described in the simulation. Thus, we cannot rely on the MC prediction for the selection efficiency for these background categories. Nevertheless, the data-MC agreement of the distribution of various DC kinematic variables is satisfactory *for each category*. This is shown using 4 variables able to discriminate between the signal and the background categories.

Therefore, we decided to simultaneously fit the number of events due to signal or to each background category using one variable at a time plotted in multidimensional independent bins of these 4 discriminating variables. The systematic uncertainty of this procedure is discussed in detail in section 4.2.

4.1 Definition of the fit procedure

Four variables are used to discriminate between signal and background.

1. The difference between missing energy and momentum $\Delta E_{\pi e} = E_{\mathrm{miss}} - cp_{\mathrm{miss}}$ is evaluated from the particle momenta reconstructed by the DC and the K_S momentum known from the K_L-*crash* tag. For $\pi^\pm e^\mp \bar{\nu}(\nu)$ decays, E_{miss} and p_{miss} are the neutrino energy and momentum, and coincide with each other. The distribution of $\Delta E_{\pi e}$ is shown in Fig. 26 after ToF cuts are imposed on $\pi^- e^+ \nu$ (left panel) and on $\pi^+ e^- \bar{\nu}$ (right panel) candidate events. A clear peak around zero is evident and corresponds to the signal for $K_S \to \pi e \nu$.

The residual background is dominated by $K_S \to \pi^+\pi^-(\gamma)$ decays. Each background event is assigned to one of the following mutually exclusive categories:

$\pi\mu(\mu\pi)$ A pion decays to a muon before reaching the tracking volume: from the MC-truth

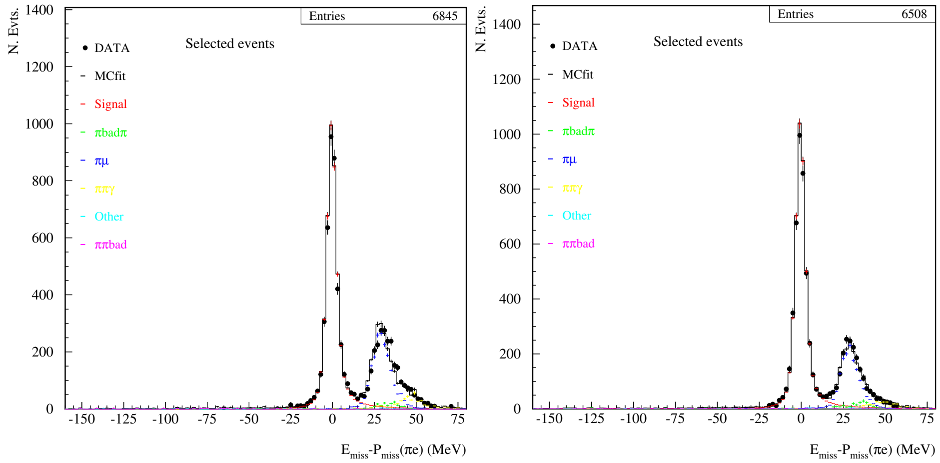

Figure 26: Distribution of $E_{\rm miss}-cp_{\rm miss}$ for $\pi^-e^+\nu$ (left panel) and for $\pi^+e^-\bar{\nu}$ (right panel) candidate events, for data of year 2002 (dots) and MC after fit (black solid line). Contributions due to signal events and to the various background categories are also shown.

is established that in the $\pi\mu(\mu\pi)$ events the main contributor to the track identified as electron (pion) by ToF is the muon;

$\pi_{\rm bad}\pi(\pi\pi_{\rm bad})$ the track identified as pion (electron) by ToF is "badly" reconstructed: the difference between its energy in the K_S frame and $M_K/2$ is larger than that calculated for the other track;

$\pi\pi\gamma$ The photon radiated at the K_S vertex has an energy in the K_S frame above 7 MeV; as a consequence the invariant mass $M_{\pi\pi}$ is below 490 MeV and $E_{\rm miss}$ is shifted toward positive values;

other $K_S\to\pi^0\pi^0$ decays with one π^0 undergoing a Dalitz decay, $K_S\to\pi\mu\nu$, or $\phi\to K^+K^-$ decays.

Events with $\Delta E_{\pi e}>10$ MeV are mostly due to radiative $K_S\to\pi e\nu$ decays, and to background categories $\pi\mu$, $\pi_{\rm bad}\pi$, and $\pi\pi\gamma$. Events with $\Delta E_{\pi e}<-10$ MeV are mostly due to resolution tails for the signal, and to background categories $\pi\mu$, $\pi_{\rm bad}\pi$, and $\pi\pi_{\rm bad}$.

2. The quality of the vertex reconstruction is checked by the difference $\mathrm{d}_{\rm PCA}=d_{\rm PCA}(1)-d_{\rm PCA}(2)$ of the impact parameters with the IP of the positive and negative charged tracks, calculated in the transverse (x,y) plane. While signal and $\pi\pi\gamma$ events peak around zero, $\pi\mu$ events show a broad peak around $\mathrm{d}_{\rm PCA}\sim 5$ cm, due to the flight path traveled by the pion before decaying, see Fig. 27.

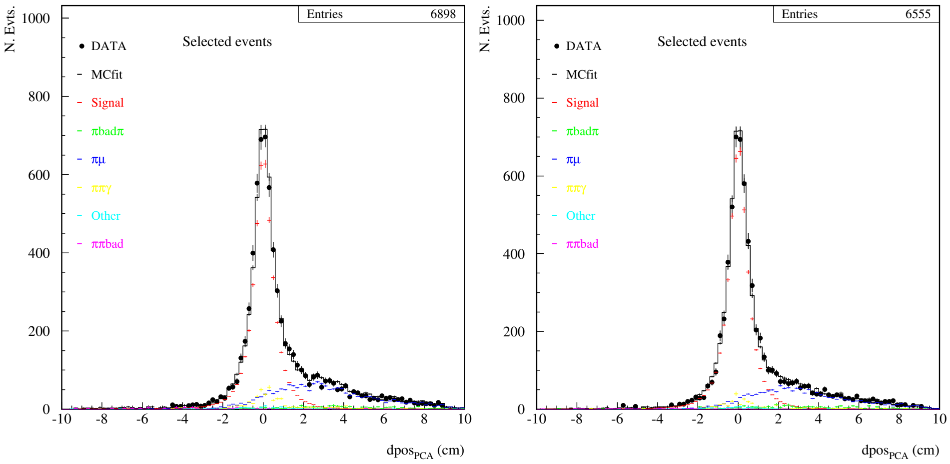

Figure 27: Distribution of the difference of the impact parameters of the positive and negative track in the transverse plane for $\pi^- e^+ \nu$ (left panel) and for $\pi^+ e^- \bar{\nu}$ (right panel) candidate events, for data of year 2002 (dots) and MC after fit (black solid line). Contributions due to signal events and to the various background categories are also shown.

3, 4. Two additional variables are used to distinguish between the various background components: the difference $\Delta E_{\pi\pi}$ between missing energy and missing momentum in the π-π hypothesis, peaking around zero for $\pi\pi\gamma$ events, see Fig. 28; the one-track square-mass M^2_μ, obtained from momentum of track 1(2) assuming that $\mathbf{p_S} - \mathbf{p_{2(1)}}$ is the momentum of an undetected pion decaying to $\mu\nu$, and that $(p_S - p_1 - p_2)^2 = 0$ for a $\pi^+\pi^-$ event. The distribution of M^2_μ for the track known as electron from ToF peaks around the muon mass squared for $\pi\mu$ events, as shown in Fig. 28.

The number of data events belonging to the $\mu\pi$ category (i.e. when the π is identified as an electron) is much higher than predicted by the MC. This is clearly shown if the energy $E^*_\pi(\mathrm{e})$ of the particle identified as electron by ToF, and the squared mass of the track known as pion from ToF are plotted (Fig. 29): the peak corresponding to monochromatic pions from $K_S \to \pi^+\pi^-(\gamma)$ at $E^*_\pi(\mathrm{e}) \sim M_K/2$ in the left panel plots, and that in the right panel plots at $M^2_\mu(\pi) \sim m^2_\mu$ due to early $\pi \to \mu\nu$ decays are practically absent in the MC. Events lying in the region

$$M^2_\mu(\pi) > 7500\,\mathrm{MeV}^2 \text{ and } |E^*_\pi(\mathrm{e}) - \mathrm{M_K}/2| < 10\,\mathrm{MeV} \tag{19}$$

are rejected, thus removing all of the events belonging to this category. The inefficiency for the signal is $1 - \epsilon_{\mu\pi} \sim 0.27\%$ and is taken from MC.

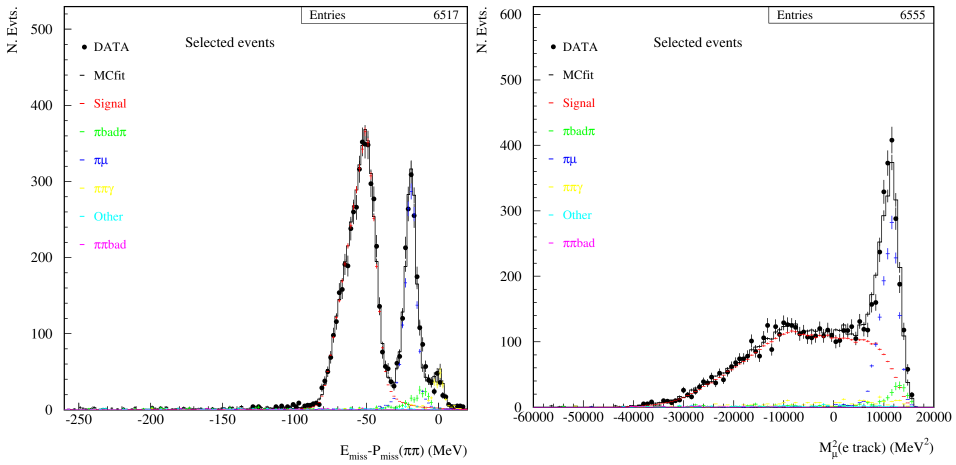

Figure 28: Left: distribution of the difference $\Delta E_{\pi\pi}$ between missing energy and missing momentum in the π-π hypothesis for $\pi^+ e^- \bar{\nu}$ candidate events, for data of year 2002 (dots) and MC after fit (black solid line). Right: distribution of the one-track square-mass M_μ^2 for the track known as electron for $\pi^+ e^- \bar{\nu}$ candidate events, for data of year 2002 (dots) and MC after fit (black solid line). Contributions due to signal events and to the various background categories are also shown.

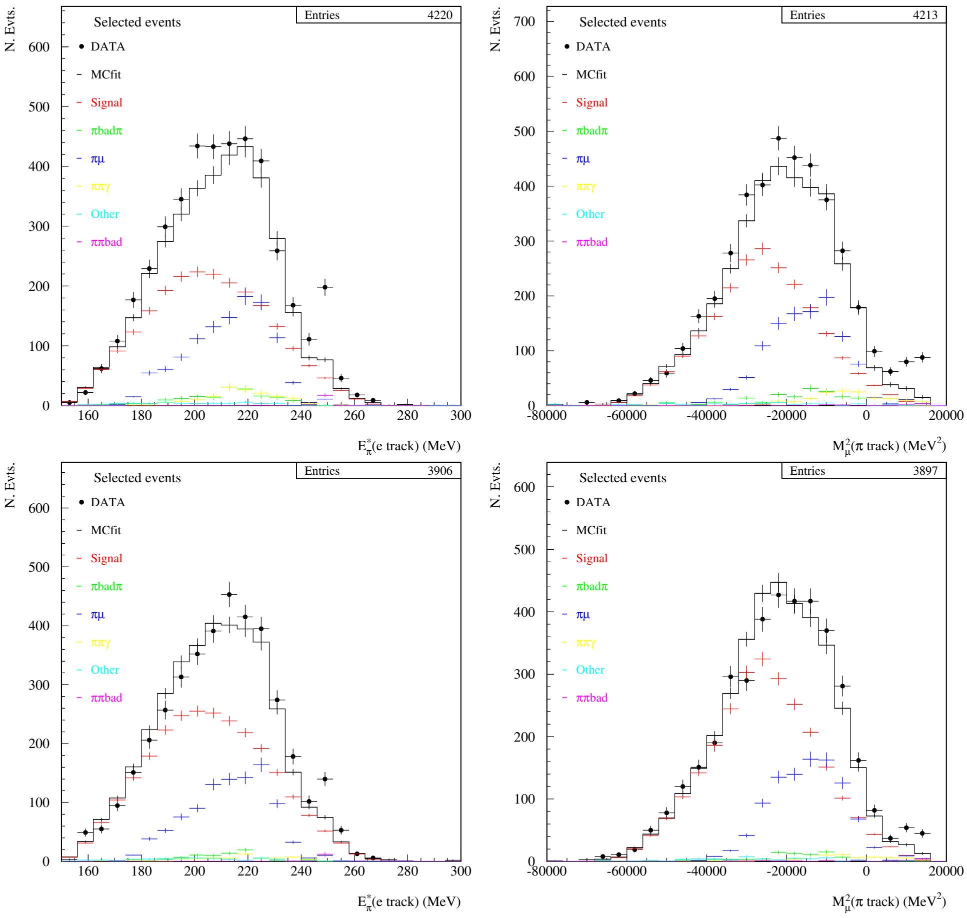

Figure 29: Left panels: distribution of the energy $E^*_\pi(\mathrm{e})$ of the particle identified as electron by ToF in the K_S frame; right panels: distribution of the square track mass $M^2_\mu(\pi)$ of the particle identified as pion by ToF in the K_S frame. Upper panels are for $\pi^- e^+ \nu$ ($\pi^+ e^- \bar{\nu}$) candidate events, for data of year 2001 (dots) and MC after fit (black solid line). Contributions due to signal events and to the various background categories are also shown.

4.1.1 Fit procedure

After the previous cut, we are left with 6 unknowns: the number of signal events and of the events of the 5 categories of background: $\pi\mu$, $\pi_{\rm bad}\pi$, $\pi\pi_{\rm bad}$, $\pi\pi\gamma$, and other. We aim at determining these by a unified binned-likelihood fit to the four variables discussed above. In order to obtain a good separation of one peaking component with respect to the others, we exploit the information coming from the variables $\mathrm{d}_{\rm PCA}$ and $\Delta E_{\pi e}$. Each event is assigned to one out of 5 regions in the $\Delta E_{\pi e}$-$\mathrm{d}_{\rm PCA}$ plane; the definition of the regions, labeled from 1 to 5, is graphically shown in Fig. 30. For each region, we use for the fit one

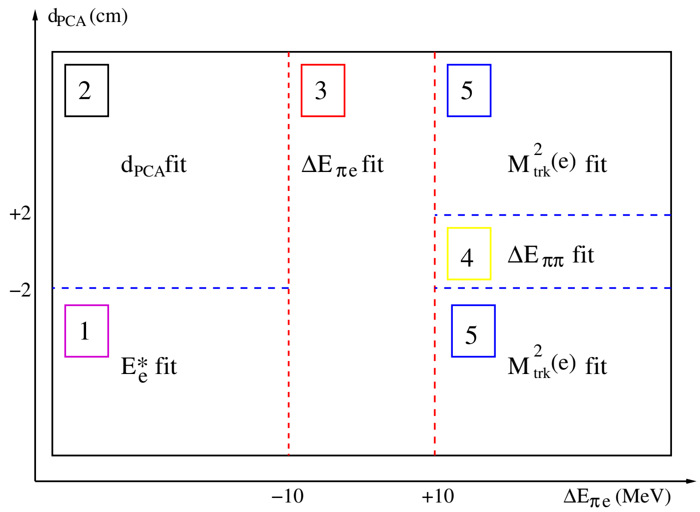

Figure 30: Definition of the fit regions in the $\Delta E_{\pi e}$-$\mathrm{d}_{\rm PCA}$ plane. In each region, the variable used for the fit ("view") is also written; an example of the distribution after the fit is shown in Fig. 31 and Fig. 32.

of the 4 variables defined above ("view"), as shown in Fig. 31 and Fig. 32. The definition of the various "views" are the following:

- $E^*_\pi(\mathrm{e})$ in region 1, where the $\pi_{\rm bad}\pi$ component has a peak around $M_K/2$;
- $\mathrm{d}_{\rm PCA}$ in region 2, where the left tail of $\Delta E_{\pi e}$ for the signal peaks around zero;
- $\Delta E_{\pi e}$ in region 3, where the signal peaks around zero;

- $\Delta E_{\pi\pi}$ in region 4, where $\pi\pi\gamma$ events peak around zero;
- $M_\mu^2(\pi)$ in region 5, where the $\pi\mu$ component peaks around M_μ^2.

The fit is performed simultaneously over the 5 regions, by maximizing the following likelihood function:

$$\mathcal{L} = \prod_{i=1}^{5} \prod_{j=1}^{n(i)} L\left(d_j(i), m_j^{(k)}(i); p_k\right) \tag{20}$$

where the index i runs over the five regions; j runs over the bin of the variable chosen in the i^{th} region; k is one of the 6 fit components. In the above formula, d and $m^{(k)}$ are the contents for data and for the k^{th} MC component, respectively. The finite statistics of the MC components is taken into account in the definition of the probability L, as explained in [9]. The log-likelihood is normalized in order to obtain a chi-square distributed variable, as explained in [8]. The fit parameters are the 6 normalizations, p_k.

The *other* component is not peaking in any of the regions; the total population of this component is estimated by MC to be $\sim 1\%$ of the signal counts, so we decided to fix it to the MC prediction.

The population of the $\pi_{\text{bad}}\pi$ component is $\sim 0.5\%$ of the signal and peaks in region 1. Due to the poor statistics of the MC distribution for this component, if the corresponding normalization is left free in the fit we observe a convergence to a huge unreasonable value: the fit is guided by the fluctuations of more abundant components. This behavior is allowed by the inclusion of the MC fluctuations in the fit function. We then decided to estimate the normalization for this component in a previous stage, performing a fit without taking into account the finite MC statistics, namely minimizing a usual χ^2 function. This component is then fixed in the final likelihood-fit.

The results for each charge final state and for each year of data taking are summarized in Tab. 10. The distributions obtained after the fit for each of the 5 regions and the plot of the residuals are shown in Fig. 31 and Fig. 32.

4.1.2 Shape correction

An evident lack of events is observed in region 2 and is concentrated for $\mathrm{d_{PCA}} \sim 0$, where the only peaking component is the signal. We addressed the nature of the missing events by looking to the properties of the cluster known as electron from ToF. We defined a PID function based on the spatial distribution of the energy in the EmC, exploiting control samples of electron, pion, and muon clusters, as usual distinguishing for the particle charge and detector. A binned likelihood $P(e, \pi, \mu)$ is defined for each particle type, equal to the normalized distribution of the ratio $E_{\text{cl}}/p_{\text{trk}}$ of cluster energy and track momentum

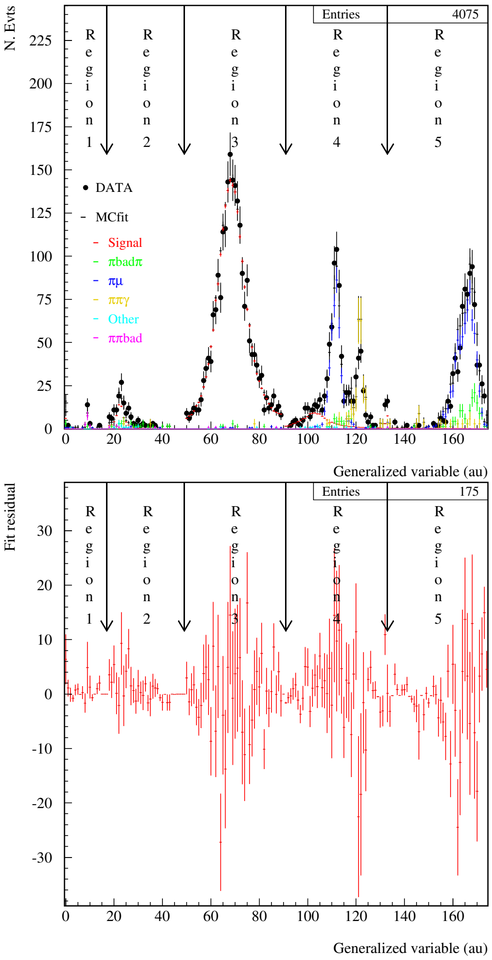

Figure 31: Distributions after the likelihood fit, for charge $\pi^- e^+ \nu$ and year 2001. Upper: result of the likelihood fit, where dots represent data, the black solid line represents the fit result. Contributions due to signal events and to the various background categories are also shown. Lower: plot of the fit residuals.

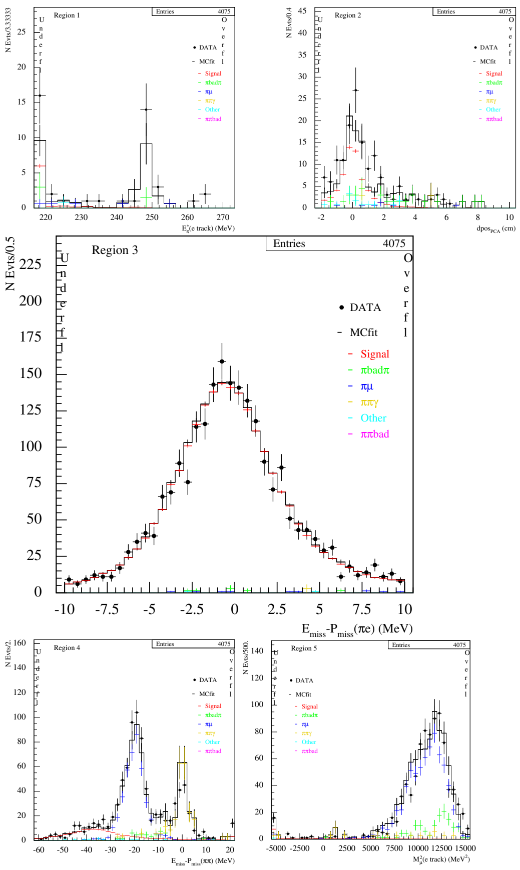

Figure 32: Distributions after the likelihood fit, for charge $\pi^- e^+ \nu$ and year 2001. Zoom of the fit result for the various regions of the d_{PCA}-$\Delta E_{\pi e}$ plane. In each region, contents of the first (last) bin are the histogram underflows (overflows).

Year	2001		2002	
Charge	$\pi^- e^+ \nu$	$\pi^+ e^- \bar{\nu}$	$\pi^- e^+ \nu$	$\pi^+ e^- \bar{\nu}$
signal	2376(52)	2529(53)	4211(69)	4412(70)
$\pi\pi_{\rm bad}$	334(61)	121(38)	435(75)	561(82)
$\pi\mu$	1039(64)	976(50)	1717(77)	1353(72)
$\pi\pi\gamma$	268(39)	155(28)	404(41)	172(24)
$\pi_{\rm bad}\pi$	27.5(5.2)	28.3(5.3)	30.8(5.6)	29.2(5.4)
other	20.3(4.5)	6.6(2.6)	54.8(7.4)	21.8(4.7)
χ^2/n.d.f.	196/166 (5.7%)	153/170 (83%)	212/170 (1.6%)	172/169 (43%)

Table 10: Result of the binned-likelihood fit the 2001-2002 data set. The values within the parentheses in the last line are the residual χ^2 probabilities.

as a function of the cluster depth $d_{\rm long}$. A different function is obtained for different values of the momentum, in 20- MeV bins. Examples of these distributions are shown in Fig. 33. The PID function is defined as

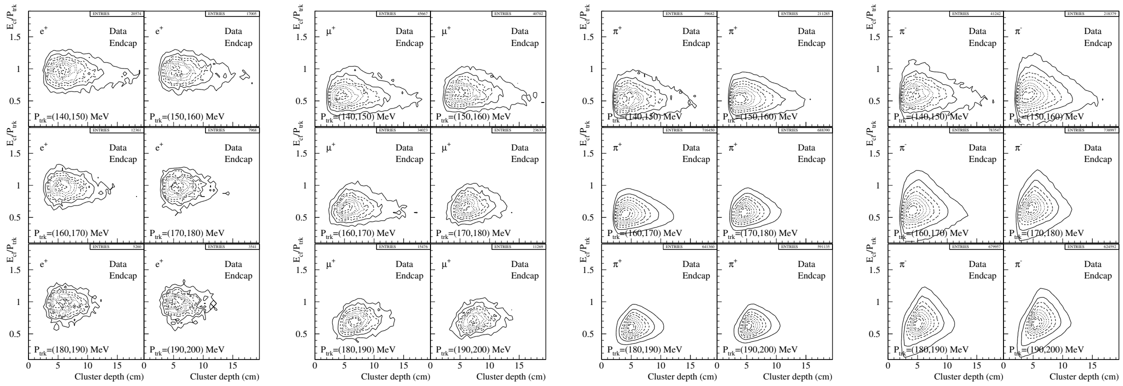

Figure 33: Distributions of the ratio $E_{\rm cl}/p_{\rm trk}$ of cluster energy and track momentum vs the depth of the cluster centroid, for tracks with impact on the calorimeter endcaps, and for different values of $p_{\rm trk}$. The 15 contours shown are equally spaced in z.

$$\mathrm{PID}(E/p, d_{\rm long}; p) = 2 - 2\frac{\log P(e)}{\log \max\{P(\pi), P(\mu)\}}.$$

Since the MC simulation is not reliable in reproducing the distributions for $E_{\rm cl}/p_{\rm trk}$ and for the cluster depth, in order to obtain the PID variable in a MC event we developed an *ad-hoc* simulation based on the distributions from data. This simulation only relies on the value of the track momentum on an event-by-event basis. The distribution of the PID variable for events lying in region 2 is shown in Fig. 34, where the MC components are normalized using the output of the fit. The lack of events is concentrated around 1, where the signal peaks. This confirms the electron assignment from the ToF. Possible

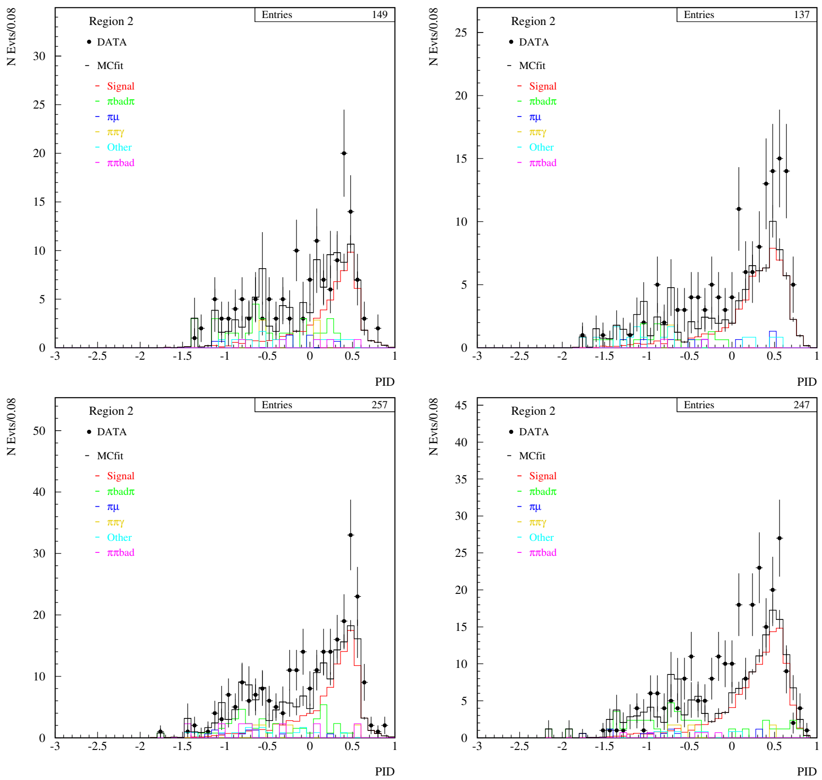

Figure 34: Distributions of the PID variable for events lying in region 2 of the $\mathrm{d_{PCA}}$-$\Delta E_{\pi e}$ plane. Upper (lower) plots are obtained for charge $\pi^- e^+ \nu$ (left) and $\pi^+ e^- \bar{\nu}$ (right) of year 2001 (2002). The MC distribution are obtained using the weights output from the likelihood fit. Dots represent data, the black solid line represents the fit result. Contributions due to signal events and to the various background categories are also shown.

sources of events not included in the "official" simulation, having a good quality vertex ($\mathrm{d_{PCA}} \sim 0$) and electron tracks have been considered, such as the contributions from secondary $\pi \to e\nu$ decays and $K_S \to \pi^+\pi^- e^+ e^-$ decays; these contributions, anyway, turn out to be completely negligible, as proved by running dedicated MC simulations.

Charge	Year	N(multi fit)	N(PID fit)	δN	$1 + \delta N/N$(multi fit)
$\pi^- e^+ \nu$	2001	59.7(1.3)	67(17)	+7(17)	1.11(0.28)
$\pi^+ e^+ \bar{\nu}$	2001	61.7(1.3)	120(13)	+58(13)	1.94(0.21)
$\pi^- e^+ \nu$	2002	105.3(1.7)	172(18)	+66(18)	1.63(0.17)
$\pi^+ e^+ \bar{\nu}$	2002	111.4(1.8)	182(19)	+70(19)	1.64(0.17)
Average weight					1.638(0.097)

Table 11: The number of events in region 2 from the multi-component likelihood fit is compared with that obtained from a two-component fit to the PID distribution. The quantity $1 + \delta N/N = 1 + (N(\text{PID fit}) - N(\text{multi fit}))/N$ represents the enhancement factor for the signal tail populating region 2.

The remaining explanation is that the lack of events is due to badly simulated tracking resolution tails for the signal. This is also suggested by the study of $K_S \to \pi^+\pi^-(\gamma)$ events selected after a K_L crash tag is required. The disagreement of the shapes between data and MC in the left tail of $\Delta E_{\pi\pi}$ is of the same order of magnitude as that observed for the left tail of $\Delta E_{\pi e}$ for $K_S \to \pi e \nu$ candidate events; the fraction of events with $\Delta E_{\pi\pi} < -10\,\text{MeV}$ is $\sim 20\%$ higher for data than for MC. In order to estimate the amount of the effect for $K_S \to \pi e \nu$, we performed an independent fit to the distributions of the PID variable for events in region 2, leaving free the normalization for the signal and the background, while retaining the weights of the various background components as output of the previous fit procedure. The fit output is the number of missing signal events, shown in Tab. 11. This procedure has been applied using other variables, such as δt_e or $\mathrm{d}_{\mathrm{PCA}}$, yielding similar results for the enhancement factors $\delta N/N$. Moreover, if this independent fit is applied to region 3, 4, and 5, we never observe correction factors different from 1 for more than 2 standard deviations. In order to correct for this effect we *averaged* these fractions for the two charges of the final state and for the two years of data taking; we then corrected the shapes of the signal distributions accordingly, for regions 1 and 2, and we repeated the fit described in the previous section. The results obtained are shown in Tab. 12.

Since we were not able to reproduce the effect using the simulation from first principles, we conservatively decided to use as final estimate for the number of signal events the average of the values shown in Tab. 10 and Tab. 12; the systematic uncertainty related to this shape correction is taken as half the difference of the values, see Tab. 13. Both the fraction of events in the left tail of $\Delta E_{\pi e}$ and the entity of the correction change significantly as a function of the K_L crash energy cut. If the energy of K_L cluster is lower, an event tagged as a K_L crash can actually be a late K_L decay happened before entering the

Year	2001		2002	
Charge	$\pi^- e^+ \nu$	$\pi^+ e^- \bar{\nu}$	$\pi^- e^+ \nu$	$\pi^+ e^- \bar{\nu}$
signal	2398(53)	2553(53)	4266(69)	4481(70)
$\pi\pi_{\mathrm{bad}}$	445(78)	80(47)	317(73)	297(54)
$\pi\mu$	981(70)	1002(54)	1793(78)	1493(64)
$\pi\pi\gamma$	201(28)	155(29)	409(42)	227(30)
$\pi_{\mathrm{bad}}\pi$	27.5(5.2)	28.3(5.3)	30.8(5.6)	29.2(5.4)
other	18.1(4.3)	6.3(2.5)	49.8(7.1)	19.8(4.5)
χ^2/n.d.f.	193/166(7.3%)	145/170(91%)	200/170(5.7%)	171/169(44%)

Table 12: Result of the binned-likelihood fit the 2001-2002 data set, after the shape correction has been applied to the signal distribution. The values within the parentheses in the last line are the residual χ^2 probabilities.

calorimeter. A sample selected with a looser K_L crash energy cut is therefore different with respect to that for a tighter cut for the following aspects: the resolution on the K_L direction reconstructed from the cluster position has non-Gaussian tails and this affects p_{miss} more than E_{miss}; the reconstruction interference between tracks from K_S and backward emitted K_L tracks is enhanced, as discussed in Sec. 3.1. This last effect is not well simulated by the MC, as observed in the measurement of the ratio of BR's for $K_S \to \pi^+\pi^-(\gamma)$ and $K_S \to \pi^0\pi^0$ [17]. Enhancement factors and shape corrections relative to three values of the crash minimum energy are listed in Tab. 13. If the cut is moved from 200 MeV to 125 MeV, the shape correction passes from ~ 0.4 standard deviations for the signal to ~ 0.9, while is statistically negligible if the cut is put at 300 MeV. The study of the stability of the result as a function of the K_L crash energy cut, discussed in the following section, is a relevant check of the reliability of the shape correction.

4.2 Systematic uncertainties

The first basic problem we addressed concerns the reliability of the fit procedure. Studying the fit response on distributions from toy-MC, we have tested the statistics distribution of the log-likelihood, the distribution of the fit estimates for the parameters p_k, and the reliability of the error estimated on the p_k. We generated samples of different statistics distributed as the sum of 2, 3, and 4 Gaussian partially overlapping. We then performed likelihood and chi-square fits, leaving as free parameters the normalization of each Gaussian. Two examples of these fits are shown in figure Fig. 35. Each cycle of generation and fit is repeated 500 times.

Crash energy cut 125 MeV		Average weight 1.692(59)	
Charge	Year	$\frac{N(\text{shape corr})-N(\text{no corr})}{N(\text{no corr})}$	$\frac{N(\text{shape corr})-N(\text{no corr})}{\sigma N(\text{no corr})}$
$\pi^- e^+ \nu$	2001	2.27%	1.07
$\pi^+ e^+ \bar{\nu}$	2001	1.31%	0.70
$\pi^- e^+ \nu$	2002	1.29%	0.89
$\pi^+ e^+ \bar{\nu}$	2002	1.13%	0.80
Crash energy cut 200 MeV		Average weight 1.638(97)	
Charge	Year	$\frac{N(\text{shape corr})-N(\text{no corr})}{N(\text{no corr})}$	$\frac{N(\text{shape corr})-N(\text{no corr})}{\sigma N(\text{no corr})}$
$\pi^- e^+ \nu$	2001	0.46%	0.21
$\pi^+ e^+ \bar{\nu}$	2001	0.47%	0.23
$\pi^- e^+ \nu$	2002	0.66%	0.40
$\pi^+ e^+ \bar{\nu}$	2002	0.78%	0.45
Crash energy cut 300 MeV		Average weight 1.13(0.11)	
Charge	Year	$\frac{N(\text{shape corr})-N(\text{no corr})}{N(\text{no corr})}$	$\frac{N(\text{shape corr})-N(\text{no corr})}{\sigma N(\text{no corr})}$
$\pi^- e^+ \nu$	2001	0.07%	0.02
$\pi^+ e^+ \bar{\nu}$	2001	0.06%	0.02
$\pi^- e^+ \nu$	2002	0.08%	0.03
$\pi^+ e^+ \bar{\nu}$	2002	0.07%	0.03

Table 13: The fractional shape correction and the correction in σ-units are listed for the two charges of the final state, for the two year of data taking, and for three values of the K_L crash minimum energy. The quantity $(N(\text{shape corr}) - N(\text{no corr}))/N(\text{no corr})$ represents the systematic error due to uncertainties in the signal shape, too.

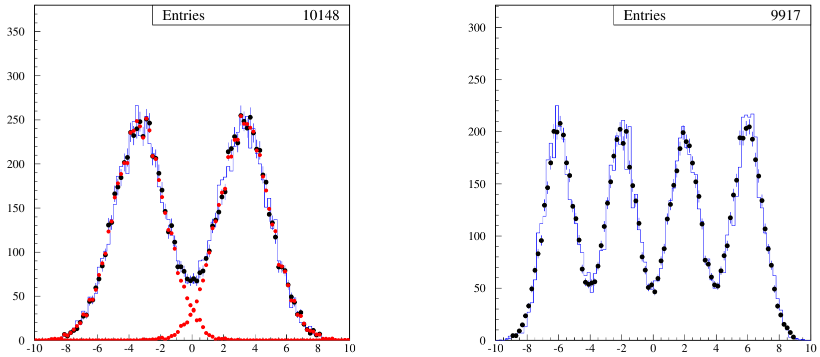

Figure 35: Distribution from toy-MC simulations. Distribution for “data” (black dots) are sampled from the sum of 2 (left) or 4 (right) Gaussian with the same integrals. The “MC” components are also sampled, from the single Gaussian. The result of likelihood fits is also shown as solid line.

The output parameters from the chi-square fit tend to be underestimated, so that the total normalization of the “data” is higher than that of the “MC”. The normalization is instead automatically preserved by the likelihood fit by construction. If there are not empty bins, both chi-square and likelihood variables follow a chi-square statistics with a number of degrees of freedom equal to the number of bins minus the number of parameters. The expectation value for the estimates of the parameters is equal to the true value, while the error estimate from the fit is slightly overestimated.

Complications arise if there are bins for which $d_j(i) \neq 0$ but $m_j^{(k)}(i) = 0$ for some k or in general there is a very low statistics: the likelihood maximum is obtained for values of the estimated MC contents which depend on the relative weights of the MC components; as a consequence of this, the distribution of the output parameters can show a dip around the expected value.

The effect of empty bins does not introduce significant shifts in the estimates from year-by-year data sets. In order to prove this and to check the reliability of the shape correction, we performed the following tests:

- We changed the bin definition of the histogram to be fit, using a variable binning: more coarse in the region of the tails and thinner in the region of the peaks. In consequence of this redefinition, the number of bins goes from 175 to 63 bins in

Year	2001		2002	
Charge	$\pi^- e^+ \nu$	$\pi^+ e^- \bar{\nu}$	$\pi^- e^+ \nu$	$\pi^+ e^- \bar{\nu}$
signal(normal binning)	2376(52)	2529(53)	4211(69)	4412(71)
signal(coarse binning)	2387(52)	2530(53)	4209(69)	4422(70)

Table 14: Number of signal events from the fit to the 2001-2002 data sets, without any shape correction applied to the signal distribution. The new binning definition for the input histograms ("coarse binning") has been changed with respect to that of Tab. 10 ("normal binning"): a variable binning is used and the total number of bins is 63.

total. We repeated the fit, either applying or not the shape correction to the signal, see Tab. 14. There are no significant variations in the results, with respect to the original fit.

- We divided the data set into 17 segments, according to the definition of Tabs. 1, 2 and 3. For each segment, we fit the distribution for data using as MC input for the background that of the year of belonging. We performed a stability study for the results, again changing the K_L crash energy cut. Notably, the results based on the "year-based" fit are close to that obtained for the much thinner segmentation, see Tab. 15. This would not be true if the MC background distributions relative to the same segment of the data set had been used: in that case, a good agreement is obtained only for crash energy cut of 125 MeV, while a -1% and -4% variations are observed for 200 MeVand 300 MeVcuts. The origin of the variation is the poor statistics of the MC distributions for the background, the same effect observed using toy MC's.

- In order to compare the results for the three chosen K_L-crash energy cuts, we divided the data set of each year into three homogeneous samples and we applied a different energy cut to each of these. We obtained three statistically-independent results for the branching ratios per charge, for the charge asymmetry, and for the total branching ratio, see Fig. 36. The χ^2 values are good in every case, thus confirming the stability as a function of the K_L-crash minimum-energy cut.

Another important check aims at determining possible dependences of the result with the ratio $R_{B/S}$ of the number of background events with respect to the number of signal events present in the distribution fit. We divided the entire data set into 17 subsamples, and we run the analysis individually in each sample. Except for one subsample in which the EmC

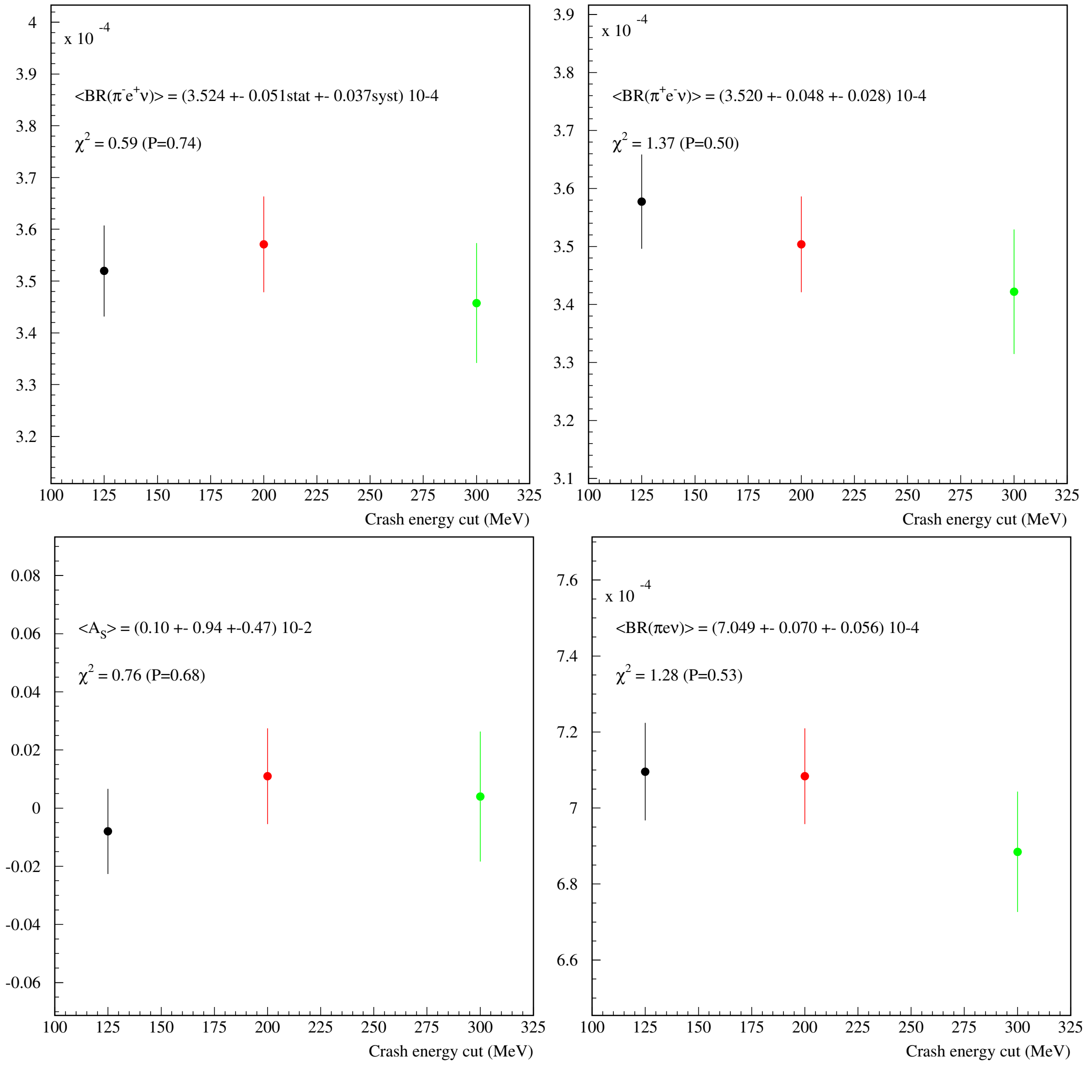

Figure 36: Results from the analysis of three statistically independent samples of data. A different minimum energy of the K_L-crash is required for each sample. For each quantity, the average of the three results and the associated χ^2 probability are shown.

Method	Year-based fit		17-data-segment fit	
	Result	Stability χ^2/ 1 dof	Result	Stability χ^2/16 dof
$\mathrm{BR}(K_S \to \pi^- e^+ \nu)\times 10^4$	3.54(6)	0.009(92%)	3.55(6)	0.56(90%)
$\mathrm{BR}(K_S \to \pi^+ e^- \bar{\nu})\times 10^4$	3.53(5)	0.33(56%)	3.54(5)	0.79(68%)
Asymmetry$\times 10^3$	1(10)	0.26(61%)	1(10)	0.88(58%)

Table 15: Results from the fit of 2001 and 2002 data sets are compared with those from the fit of 17 subsamples of the data set. The stability of the results is represented by the χ^2 probabilities shown between parentheses.

time scale was not calibrated and $R_{B/S} > 1$, in all of the samples the ratio $R_{B/S}$ ranges from 0.5 to 0.7. No significant dependency of the result from $R_{S/B}$ is observed.

Finally, as a last check of the fit reliability, we compared the distribution of many variables not directly used in the fit for data and MC, using the normalization output of the fit. We show in Fig. 37 the distributions of the PID variable, of the muon square masses for pion tracks $M_\mu^2(\pi$ track), of the energy of the pion tracks boosted in the K_S rest frame using the pion hypothesis $E_\pi^*(\pi$ track), of the track invariant mass $M_{\pi\pi}$, and of the track momenta of the electron and pion tracks P_e and P_π.

In all of the cases, data well agrees with the MC normalized according to the fit output. We underline that the PID variable depends on the cluster properties and therefore it's completely independent of the track momenta used for the definition of the variables actually used in the fit; the invariant mass $M_{\pi\pi}$ depends on the track momenta, but it's independent of the K_L-momentum determined from the K_L-crash cluster direction.

4.3 Determination of the form factor slope parameter λ_+

The small number of $K_S \to \pi e \nu$ events doesn't allow us to measure the parameters of the semileptonic form factor with an accuracy comparable with that obtained with K_L decays. However, we think it is worth doing this measurement with the K_S since nobody has ever done it before and since it can only be done at a ϕ-factory. Moreover, in the MC, we use the same amplitude parametrization for semileptonic decays of K^0 and $\overline{K^0}$, as expected if T and CPT symmetries hold. By measuring the parameters of the form factor we can directly check this assumption.

The fit to the slope parameter is very sensitive to the presence of residual background, hence we applied tighter cuts on the transverse vertex position, ρ_{VTX}, and on the $\Delta E_{\pi e}$

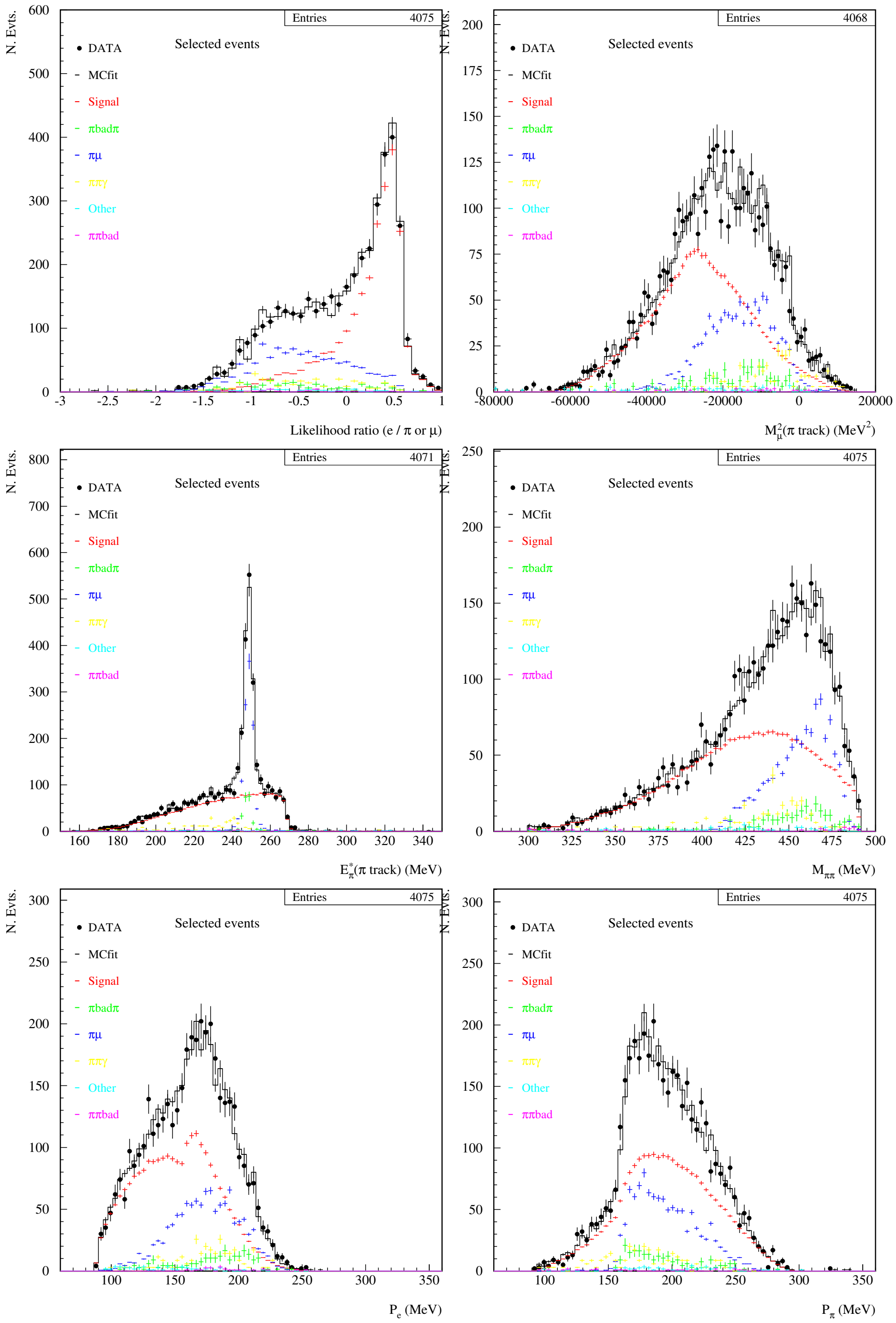

Figure 37: Distributions for charge $\pi^- e^+ \nu$ and year 2001, for data (filled dots) and MC (solid black line), of various variables. The MC is normalized according to the fit output. Contributions due to signal events and to the various background categories are also shown in various colors.

variable:

$$\begin{aligned}\rho_{VTX} &< 2\text{ cm}\\ |\Delta E_{\pi e}| &< 10\text{ MeV}.\end{aligned}$$

We also loose the energy requirement on the K_L-crash to 110 MeV. About 15000 signal events survives this selection, combining the data for the two years and charge modes, and the fraction of background events is reduced to 0.7%. The distributions of the transferred momentum $t = |P_K - P_\pi|^2$ for data and MC events are shown in Fig. 39. The distribution for the data is shown after the subtraction of the background, as obtained from the MC, and weighted according to the results of the fit discussed in the previous sections: first the MC background subtraction is done for each year and charge mode separately, and then the data distributions are added together. The MC signal distribution is obtained by weighting each MC event with the ratio of data and MC efficiencies as obtained for that event. The ratios of data and MC efficiency as a function of $t/m^2_{\pi+}$ are shown Fig. 38 for the two years of data taking and for the two charge modes.

In the MC simulation the form factor is parametrized as:

$$f_+(t)/f_+(0) = 1 + \lambda_{+,MC} t/m^2_{\pi+},$$

where $\lambda_{+,MC} = 0.03$. In order to evaluate the slope λ_+ in the data, we fit the ratio of data and MC $t/m^2_{\pi+}$-distributions with the function:

$$F(t) = A \times \left(\frac{1 + \lambda_+ t/m^2_{\pi+}}{1 + \lambda_{+,MC} t/m^2_{\pi+}}\right)^2,$$

where A and λ_+ are the free parameters of the fit. The fit to the ratio of the two distributions is shown in Fig. 40. We obtain for the linear slope of the K_S semileptonic form factor:

$$\lambda_+ = (33.9 \pm 4.1) \times 10^{-3}, \tag{21}$$

with $\chi^2/Ndeg = 12.88/11$ corresponding to a probability $P(\chi^2) \simeq 30\%$. This result is in agreement with the corresponding value from linear fit of K_L semileptonic form factor, $(28.2 \pm 0.9) \times 10^{-3}$ [13].

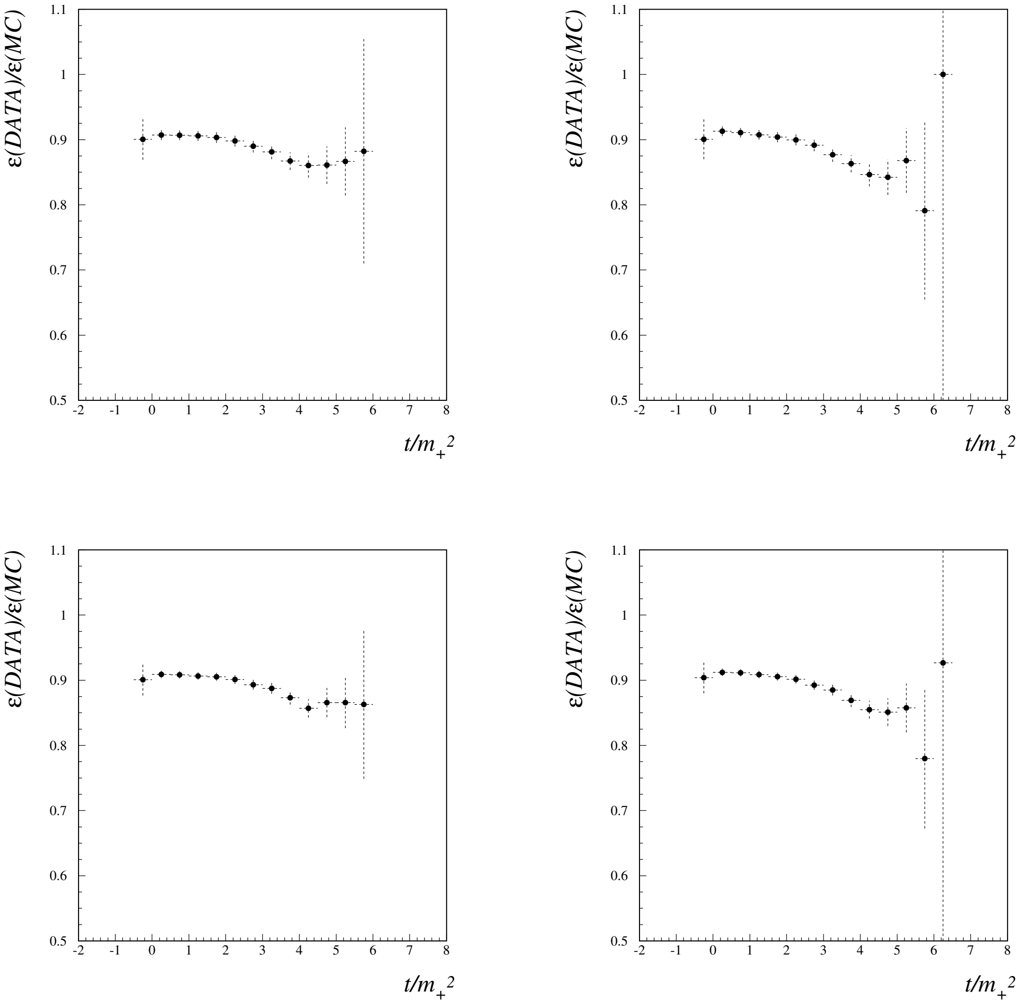

Figure 38: Ratio of data and MC efficiencies as a function of the normalized transferred momentum $t/m^2_{\pi+}$, for the year 2001 (2002) on the top (bottom) panels, and for $\pi^- e^+ \nu$ ($\pi^+ e^- \overline{\nu}$) decays in the left (right) column.

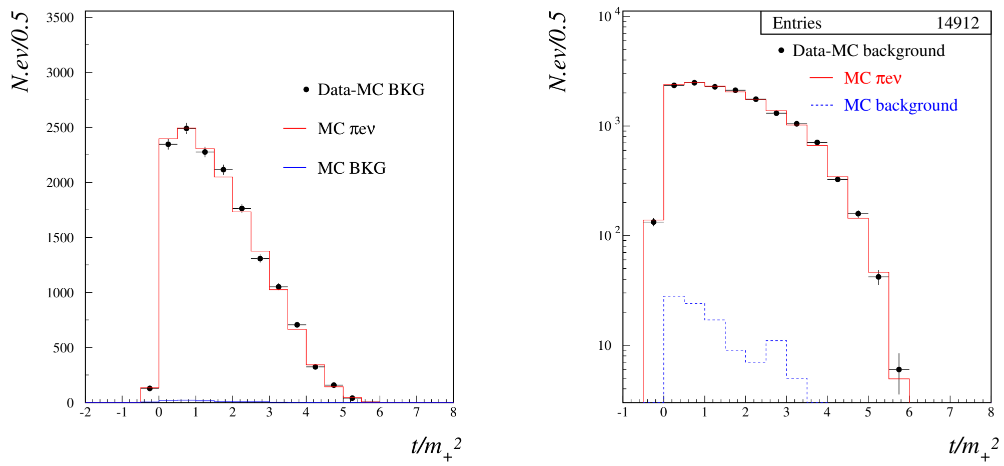

Figure 39: Comparison of data and MC distributions for the transferred momentum $t/m^2_{\pi+}$. The MC background has been subtracted to the data events. The background contamination is visible in the right plot in log scale.

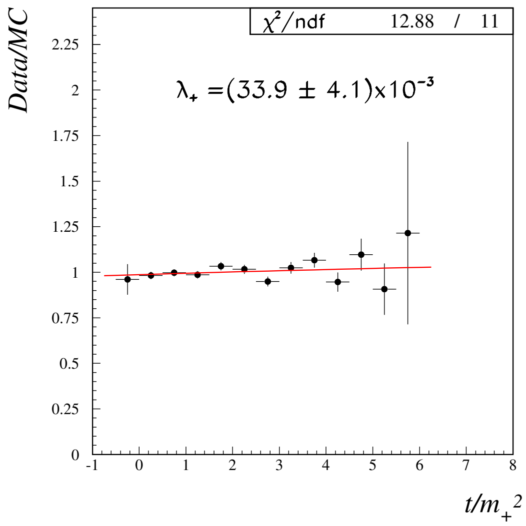

Figure 40: Fit to the ratio of data and MC $t/m^2_{\pi+}$ distributions. The result of the fit and the χ^2 are also shown.

5 Results

We obtain the ratio of BR's for semileptonic (with a chosen charge state) and $\pi^+\pi^-(\gamma)$ modes through the following formula:

$$\frac{\mathrm{BR}(K_S \to \pi^\mp e^\pm \nu(\bar{\nu}))}{\mathrm{BR}(K_S \to \pi^+\pi^-(\gamma))} = \frac{N(K_S \to \pi^\mp e^\pm \nu(\bar{\nu}))}{N(K_S \to \pi^+\pi^-(\gamma))} \times \frac{\varepsilon_{sel}(\pi^+\pi^-)}{\varepsilon_{sel}(\pi^\mp e^\pm)} \times \frac{1 - P(CV, \pi\pi)}{1 - P(CV, \pi^\mp e^\pm \nu(\bar{\nu}))} \tag{22}$$

where $N(i)$ are the number of events selected and $P(CV, i)$ is the efficiency of the cosmic veto for channel i. The number of events per pb^{-1} of integrated luminosity and the yield ratio are shown in Fig. 41 and in the left panel of Fig. 42 as a function of time. The values we used in the final analysis are those obtained for each year, which are indicated by the horizontal bands. The definition of the data periods is summarized in tables 1, 2, and 3.

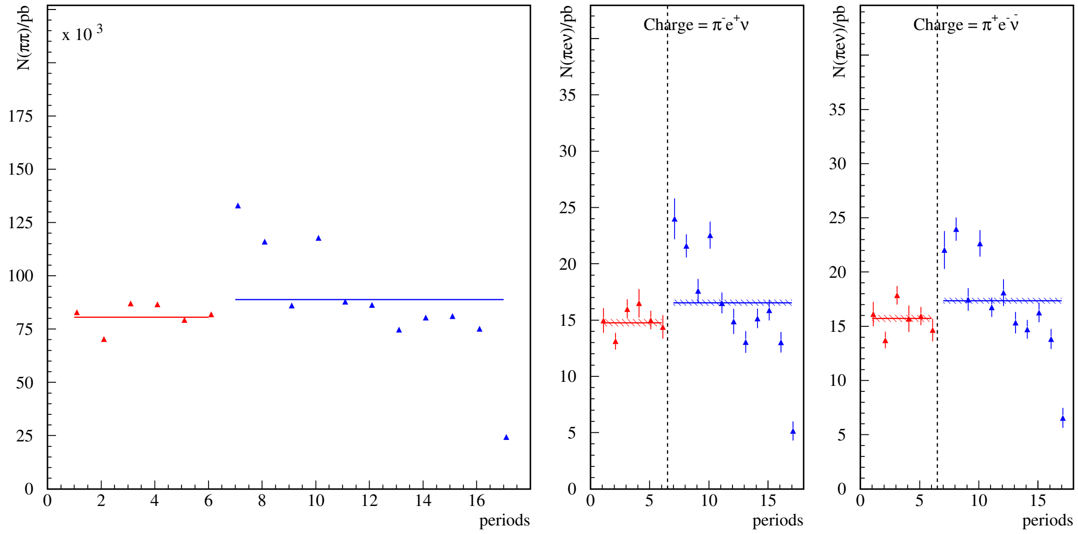

Figure 41: Number of selected events for the channels $K_S \to \pi^+\pi^-(\gamma)$ (left), $K_S \to \pi^- e^+ \nu$ (central), and $K_S \to \pi^+ e^- \bar{\nu}$ (right) per pb^{-1}, as a function of the period along the data taking. The horizontal bands represent the value for year 2001 (red) and 2002 (blue).

The expression of the selection efficiencies ϵ_{sel} (Eq. 1) is here reported:

$$\epsilon_{sel} = \epsilon_{Kcr} a_{Kcr} \sum_n T_n P_n^{in} + (1 - \epsilon_{Kcr}) a_{NKcr} \sum_n T_n P_n^{out}, \tag{23}$$

The expression for the efficiency corrections a_{Kcr} (a_{NKcr}) given the presence (absence) of a K_L-crash tag obtained with the true value of the event T_0 includes contributions for

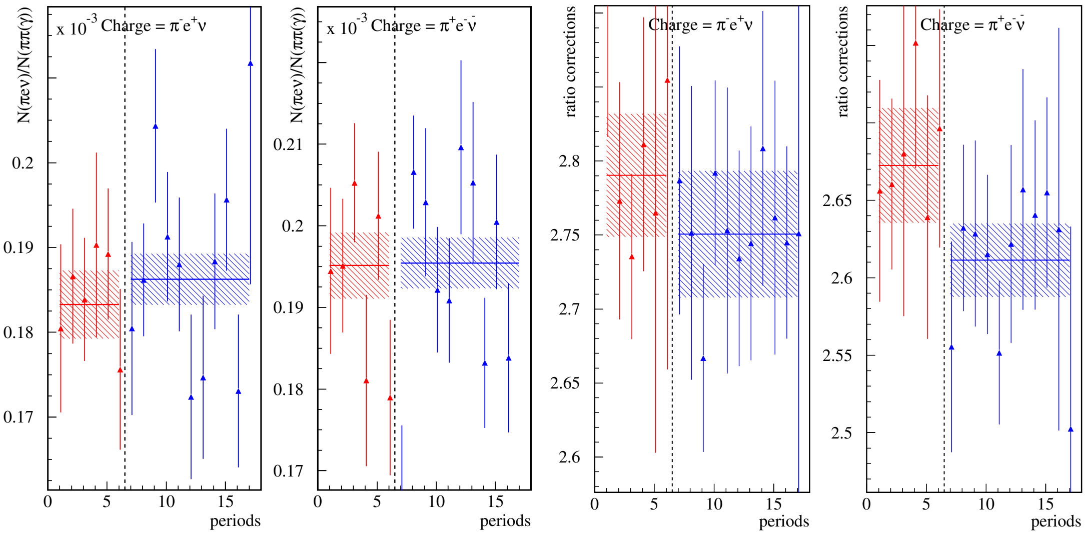

Figure 42: Ratio of the number of selected events for the channels $K_S \to \pi^- e^+ \nu$ (left), and $K_S \to \pi^+ e^- \bar{\nu}$ (central) divided by the number of selected $K_S \to \pi^+\pi^-(\gamma)$ events, as a function of the period along the data taking. Right: ratio of the selection efficiencies for $K_S \to \pi^+\pi^-(\gamma)$ and the two charge states of $K_S \to \pi e \nu$. The horizontal bands represent the value for year 2001 (red) and 2002 (blue).

each of the applied cuts. For the semileptonic channels we used the following formula:

$$a^{(\pi e\nu)} = \epsilon_{\mathrm{2trks}}\epsilon_{\mathrm{vtx}}\epsilon_{\mathrm{DCp}}\epsilon_{\mathrm{TCA}}\epsilon_{\mathrm{T0}}\sum_{n} P_n\left(\epsilon_{\mathrm{sec}}\epsilon_{\mathrm{TOF}}^{(\mathrm{sec})}T_n^{(\mathrm{sec})} + \epsilon_{\overline{\mathrm{sec}}}\epsilon_{\mathrm{Kcr}}^{(2)}\epsilon_{\mathrm{TOF}}^{(\overline{\mathrm{sec}})}T_n^{(\overline{\mathrm{sec}})}\right)\epsilon_{\mu\pi} \quad (24)$$

The methods used to evaluate the efficiency corrections for the requirements to have two tracks reconstructed from IP extrapolated to the calorimeter ($\epsilon_{\mathrm{2trks}}$), to have a vertex reconstructed (ϵ_{vtx}), to satisfy the kinematic preselection (ϵ_{DCp}), to have both tracks associated to calorimeter clusters (ϵ_{TCA}), of which at least one satisfies the golden-$T0$ cuts (ϵ_{T0}), and to have at least one trigger sector fired by the K_S clusters (ϵ_{sec}) are described in [18, 16, 26]. The efficiency correction for the cut designed to reject the $\mu\pi$-category background (Eq. 19) is evaluated using the MC. The results are summarized in Fig. 43, Fig. 44, and Fig. 45. In order to take correctly the correlations into account, we need to combine the T_n probabilities and the TOF efficiencies distinguishing whether there is a trigger sector fired from K_S or not: in the first case, there is higher probability to have particles with higher momenta, with impact on the barrel, so that the TOF efficiency is in the end higher. We show in Fig. 46 the trigger efficiency and the TOF efficiency, averaged over the possible configurations of the trigger sectors:

$$\epsilon_{trg} = \epsilon_{\mathrm{sec}} + \epsilon_{\overline{\mathrm{sec}}}\epsilon_{\mathrm{Kcr}}^{(2)} \quad (25)$$

$$\epsilon_{TOF} = \frac{\epsilon_{\mathrm{sec}}\epsilon_{\mathrm{TOF}}^{(\mathrm{sec})} + \epsilon_{\overline{\mathrm{sec}}}\epsilon_{\mathrm{Kcr}}^{(2)}\epsilon_{\mathrm{TOF}}^{(\overline{\mathrm{sec}})}}{\epsilon_{\mathrm{sec}} + \epsilon_{\overline{\mathrm{sec}}}\epsilon_{\mathrm{Kcr}}^{(2)}} \quad (26)$$

The variations of the trigger-sector and overall trigger efficiencies as a function of time (Fig. 45 and Fig. 46) are due to actual changes in the effective thresholds.

The value of the various efficiencies for each year of data are listed in Tab. 16. Efficiencies labelled "DCall" collect contributions from 2trks, VTX, and DCp efficiencies and are different according to the absence or presence of a K_L-crash tag in the event: events with prompt K_L-decays belong to the first category and can give more than one pair of tracks coming from the IP, thus being rejected by the selection strategy of Tab. 4. There is a difference between the efficiencies for each charge state: the difference between the total efficiencies given a K_L-crash tag are $0.0425 \pm 0.0099_{\mathrm{stat}} \pm 0.0057_{\mathrm{syst}}$ and $0.0505 \pm 0.0073_{\mathrm{stat}} \pm 0.0059_{\mathrm{syst}}$ for 2001 and 2002, respectively. These differences are due to the charge dependence of the TOF correction, which is a consequence of the difference between the nuclear interactions of π^+ and π^- in the calorimeter.

The expression for the $\pi^+\pi^-$ channel is simpler:

$$a^{(\pi\pi)} = \epsilon_{\mathrm{2trks}}\epsilon_{\mathrm{TCAT0}}\sum_{n} P_n\left(\epsilon_{\mathrm{sec}}T_n^{(\mathrm{sec})} + \epsilon_{\overline{\mathrm{sec}}}\epsilon_{\mathrm{Kcr}}^{(2)}T_n^{(\overline{\mathrm{sec}})}\right) \quad (27)$$

Year	2001		2002	
Charge	$\pi^- e^+ \nu$	$\pi^+ e^- \bar{\nu}$	$\pi^- e^+ \nu$	$\pi^+ e^- \bar{\nu}$
DCall	$0.3034 \pm 0.0006 \pm 0.0012$	$0.3018 \pm 0.0008 \pm 0.0012$	$0.3072 \pm 0.0007 \pm 0.0012$	$0.3050 \pm 0.0008 \pm 0.0012$
TCA	$0.92783 \pm 0.00037 \pm 0.00043$	$0.93037 \pm 0.00035 \pm 0.$	$0.9292 \pm 0.0004 \pm 0.0012$	$0.93213 \pm 0.00038 \pm 0.$
T0	$0.997165 \pm 0.000038 \pm 0.$	$0.997901 \pm 0.000026 \pm 0.$	$0.997172 \pm 0.000038 \pm 0.$	$0.997823 \pm 0.000027 \pm 0.$
TRG	$0.9360 \pm 0.0007 \pm 0.0031$	$0.93691 \pm 0.00065 \pm 0.00071$	$0.9341 \pm 0.0006 \pm 0.0036$	$0.93353 \pm 0.00064 \pm 0.$
TOF	$0.7864 \pm 0.0037 \pm 0.0007$	$0.8206 \pm 0.0033 \pm 0.0003$	$0.7913 \pm 0.0027 \pm 0.0006$	$0.8348 \pm 0.0025 \pm 0.0013$

Year	2001		2002	
Charge	$\pi^- e^+ \nu$	$\pi^+ e^- \bar{\nu}$	$\pi^- e^+ \nu$	$\pi^+ e^- \bar{\nu}$
DCall	$0.3191 \pm 0.0010 \pm 0.0013$	$0.3173 \pm 0.0011 \pm 0.0013$	$0.3240 \pm 0.0008 \pm 0.0013$	$0.3214 \pm 0.0009 \pm 0.0013$
TCA	$0.92785 \pm 0.00040 \pm 0.00047$	$0.93036 \pm 0.00036 \pm 0.$	$0.9291 \pm 0.0004 \pm 0.0013$	$0.93239 \pm 0.00041 \pm 0.$
T0	$0.997132 \pm 0.000043 \pm 0.$	$0.997867 \pm 0.000036 \pm 0.$	$0.997163 \pm 0.000040 \pm 0.$	$0.997809 \pm 0.000029 \pm 0.$
TRG	$0.9312 \pm 0.0002 \pm 0.0014$	$0.9333 \pm 0.0004 \pm 0.0012$	$0.9293 \pm 0.0003 \pm 0.0025$	$0.92978 \pm 0.00022 \pm 0.00074$
TOF	$0.7863 \pm 0.0037 \pm 0.0009$	$0.8206 \pm 0.0033 \pm 0.$	$0.7913 \pm 0.0027 \pm 0.0011$	$0.8347 \pm 0.0025 \pm 0.0012$

Table 16: $K_S \to \pi e \nu$ selection efficiencies for K_L crash energy above 200 MeV, given the absence (upper table) or presence (lower table) of a K_L-crash tag with the true value of the event T_0. Efficiencies labelled "DCall" collect contributions from 2trks, VTX, and DCp efficiencies.

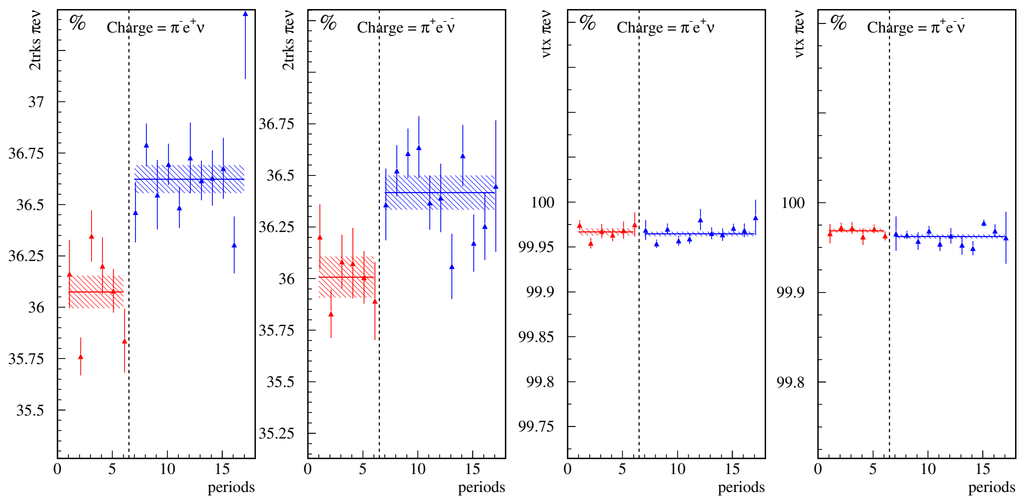

Figure 43: Efficiency to have two tracks reconstructed from the IP extrapolated to the calorimeter (2trks, left) and to have a vertex reconstructed from those two tracks (vtx, right) for $K_S \to \pi^- e^+ \nu$ and $K_S \to \pi^+ e^- \bar{\nu}$, as a function of the period along the data taking. The horizontal bands represent the value for year 2001 (red) and 2002 (blue).

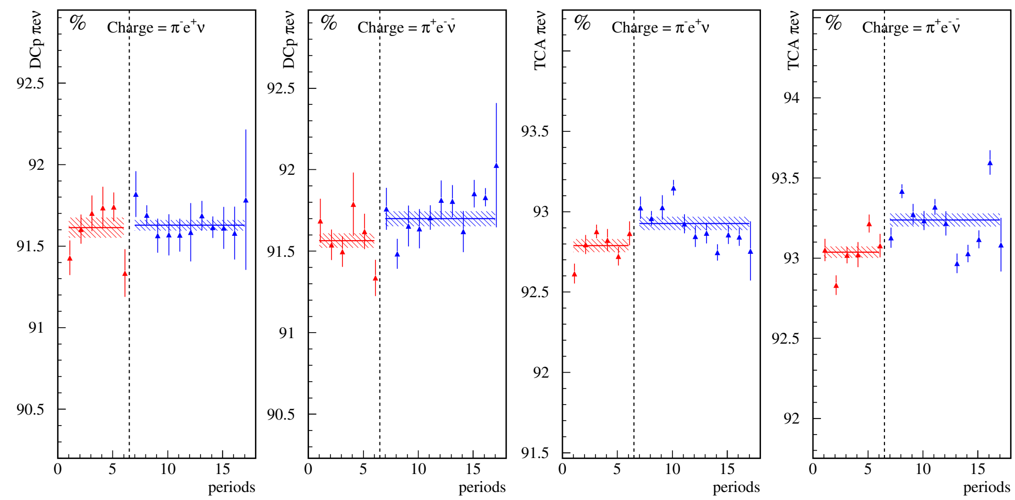

Figure 44: Efficiencies to satisfy the kinematic preselection (DCp, left) and to have two tracks associated to calorimeter clusters (TCA, right) for $K_S \to \pi^- e^+ \nu$ and $K_S \to \pi^+ e^- \bar{\nu}$, as a function of the period along the data taking. The horizontal bands represent the value for year 2001 (red) and 2002 (blue).

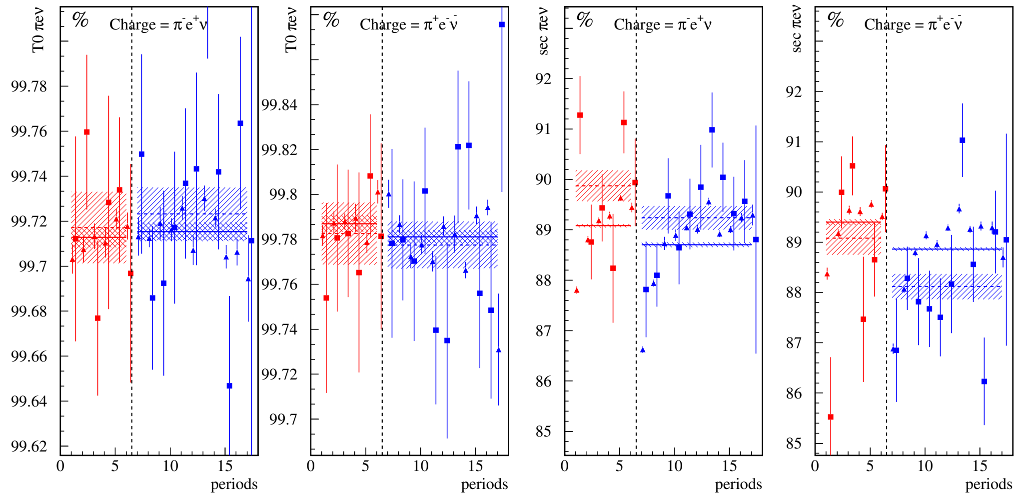

Figure 45: Efficiencies to have a golden-$T0$ cluster from the two K_S tracks (T0, left) and to fire at least one calorimeter trigger sector (sec, right) for $K_S \to \pi^- e^+ \nu$ and $K_S \to \pi^+ e^- \bar{\nu}$, as a function of the period along the data taking. Solid triangles and solid squares represent the result obtained from the single-particle and double-particle methods. The horizontal band from upper left to lower right (from lower left to upper right) represent the value for each year, from the single-particle (double-particle) methods.

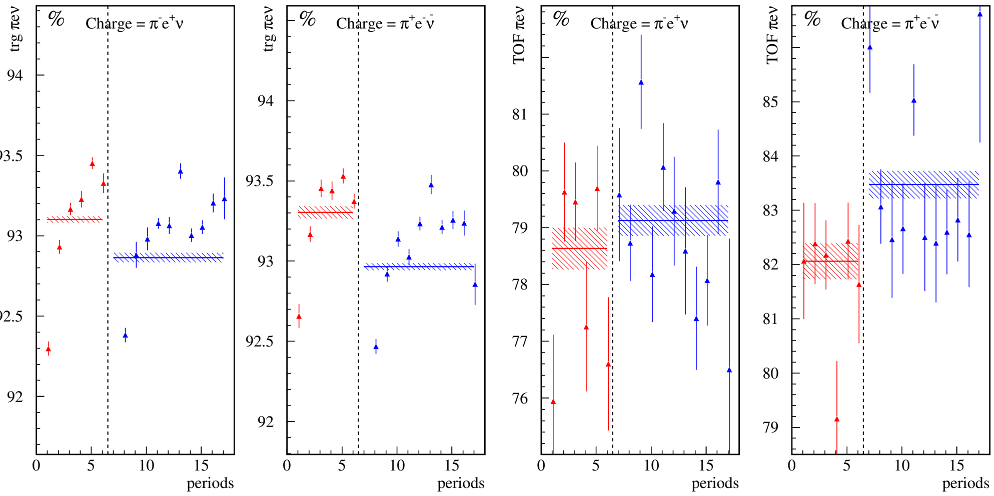

Figure 46: Trigger efficiency (left panels) and TOF efficiency (right panels) for $K_S \to \pi^- e^+ \nu$ and $K_S \to \pi^+ e^- \bar{\nu}$, as a function of the period along the data taking. The horizontal bands represent the value for year 2001 (red) and 2002 (blue).

The total corrections ϵ_{sel} for the $K_S \to \pi^+\pi^-(\gamma)$ and $K_S \to \pi e \nu$ channels are shown in Fig. 47. The ratio of these corrections are shown in the right panels of Fig. 42. By combining the values from the analysis of year 2001 and 2002, we obtain the following results for the ratio of BR's:

$$\boxed{R_{e+} = \frac{\mathrm{BR}(K_S \to \pi^- e^+ \nu)}{\mathrm{BR}(K_S \to \pi^+\pi^-(\gamma))} = (5.099 \pm 0.082_{\mathrm{stat}} \pm 0.039) \times 10^{-4}} \tag{28a}$$

$$\boxed{R_{e-} = \frac{\mathrm{BR}(K_S \to \pi^+ e^- \bar{\nu})}{\mathrm{BR}(K_S \to \pi^+\pi^-(\gamma))} = (5.083 \pm 0.073_{\mathrm{stat}} \pm 0.042) \times 10^{-4}} \tag{28b}$$

$$\boxed{\frac{\mathrm{BR}(K_S \to \pi e \nu)}{\mathrm{BR}(K_S \to \pi^+\pi^-(\gamma))} = (10.19 \pm 0.11_{stat} \pm 0.07) \times 10^{-4}} \tag{28c}$$

The correlation matrix for the statistical errors of the ratios R_{e+} and R_{e-} is diagonal, neglecting terms on the order of $1/N(K_S \to \pi^+\pi^-(\gamma))$. On the contrary, a correlation is present for the systematic errors, due to the shape correction which is common to both charges; the correlation matrix for the systematic errors is:

$$\left(\begin{array}{cc} 1 & \frac{\delta_(\mathrm{tail})(\mathrm{R_{e+}})\delta_{\mathrm{tail}}(\mathrm{R_{e-}})}{\sigma_{\mathrm{syst}}(R_{e+})\sigma_{\mathrm{syst}}(R_{e-})} \\ \frac{\delta_(\mathrm{tail})(\mathrm{R_{e+}})\delta_{\mathrm{tail}}(\mathrm{R_{e-}})}{\sigma_{\mathrm{syst}}(R_{e+})\sigma_{\mathrm{syst}}(R_{e-})} & 1 \end{array} \right) = \left(\begin{array}{cc} 1 & 0.61 \\ 0.61 & 1 \end{array} \right), \tag{29}$$

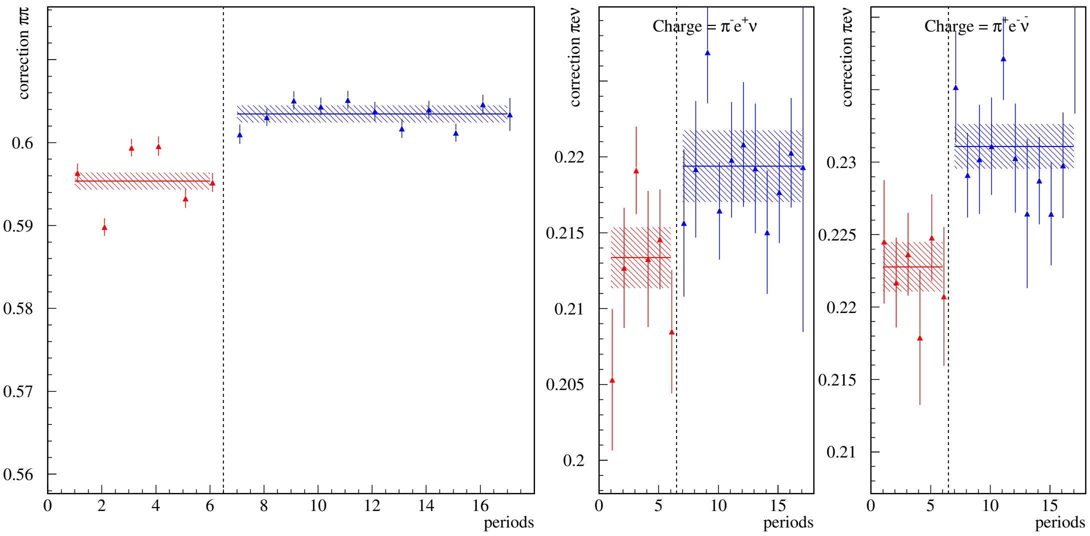

Figure 47: Starting from the left panel: total corrections for $K_S \to \pi^+\pi^-(\gamma)$, $K_S \to \pi^- e^+ \nu$ and $K_S \to \pi^+ e^- \bar{\nu}$ as a function of the period along the data taking. The horizontal bands represent the value for year 2001 (red) and 2002 (blue).

while the correlation matrix for the total errors is:

$$\begin{pmatrix} 1 & 0.13 \\ 0.13 & 1 \end{pmatrix}. \tag{30}$$

We also obtain the charge asymmetry, calculated as follows:

$$A_S = \frac{\frac{N(K_S \to \pi^- e^+ \nu)}{\varepsilon_{sel}(\pi^- e^+)(1-P(CV,\pi^- e^+ \nu))} - \frac{N(K_S \to \pi^+ e^- \bar{\nu})}{\varepsilon_{sel}(\pi^+ e^-)(1-P(CV,\pi^+ e^- \bar{\nu}))}}{\frac{N(K_S \to \pi^- e^+ \nu)}{\varepsilon_{sel}(\pi^- e^+)(1-P(CV,\pi^- e^+ \nu))} + \frac{N(K_S \to \pi^+ e^- \bar{\nu})}{\varepsilon_{sel}(\pi^+ e^-)(1-P(CV,\pi^+ e^- \bar{\nu}))}} \tag{31}$$

The results for the charge asymmetry are shown in Fig. 48 as function of the data period. Again combining results for the data set of each year, we obtain:

$$\boxed{A_S = (1.5 \pm 9.6_{stat} \pm 2.9_{syst}) \times 10^{-3}} \tag{32}$$

Here, the correlation among systematic errors for the event count of the two charges is such that the contribution from the shape correction almost cancels out.

For the sake of completeness, we show here the result for the form factor linear slope:

$$\boxed{\lambda_+ = (33.9 \pm 4.1) \times 10^{-3}} \tag{33}$$

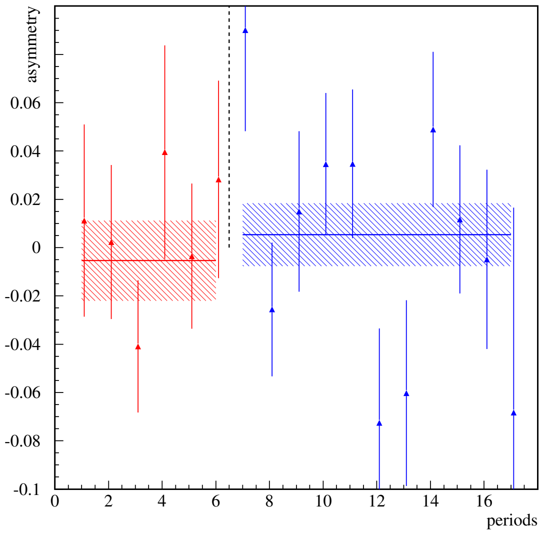

Figure 48: Results for the charge asymmetry as a function of the period along the data taking. The horizontal bands represent the value for year 2001 (red) and 2002 (blue).

5.1 Interpretation of the results

In order to evaluate the BR's for the semileptonic modes and the related $\Delta S = \Delta Q$ violating parameter, we combine the ratios of BR's measured for each charge (Eq. 28) with the ratio of BR's for $K_S \to \pi^+\pi^-(\gamma)$ and $K_S \to \pi^0\pi^0$,

$$R = \frac{\mathrm{BR}(K_S \to \pi^+\pi^-(\gamma))}{\mathrm{BR}(K_S \to \pi^0\pi^0)} = 2.2549 \pm 0.0025_{\mathrm{stat}} \pm 0.0048_{\mathrm{syst}} \text{ [17]}. \tag{34}$$

The only decay mode with a BR comparable to K_{e3} is $K_{\mu 3}$; we take it into account exploiting the universality of lepton couplings:

$$r_{\mu e} = \frac{\Gamma\,(K_S \to \pi\mu\nu)}{\Gamma\,(K_S \to \pi e\nu)} = \frac{1+\delta_K^\mu}{1+\delta_K^e}\frac{I_K^\mu}{I_K^e}, \tag{35}$$

where $\delta_K^{\mu,e}$ are mode-dependent long-distance radiative corrections and $I_K^{\mu,e}$ are decay phase space integrals. Using the KTeV measurement of $I_K^\mu/I_K^e = 0.6622(18)$ [21] and the KLOR result $(1+\delta_K^\mu)/(1+\delta_K^e) = 1.0058(10)$ [4], we get $R_{\mu e} = 0.6660(19)$. The uncertainty on the semileptonic BR's due to the BR of residual K_S decays (BR_{oth}) is given by:

$$\frac{\delta\mathrm{BR}(K_S \to \pi e\nu)}{\mathrm{BR}(K_S \to \pi e\nu)} = \frac{BR_{oth}}{1 - BR_{oth}} \sim 10^{-5}. \tag{36}$$

It is neglected in the following.

We evaluate all of the 4 main BR's of the K_S as follows:

$$\mathrm{BR}(K_S \to \pi^+\pi^-(\gamma)) = \frac{1}{1 + 1/R + (R_{e+} + R_{e-})(1 + r_{\mu e})} \tag{37a}$$

$$\mathrm{BR}(K_S \to \pi^0\pi^0) = \frac{1/R}{1 + 1/R + (R_{e+} + R_{e-})(1 + r_{\mu e})} \tag{37b}$$

$$\mathrm{BR}(K_S \to \pi^- e^+ \nu) = \frac{R_{e+}}{1 + 1/R + (R_{e+} + R_{e-})(1 + r_{\mu e})} \tag{37c}$$

$$\mathrm{BR}(K_S \to \pi^+ e^- \bar{\nu}) = \frac{R_{e-}}{1 + 1/R + (R_{e+} + R_{e-})(1 + r_{\mu e})} \tag{37d}$$

We obtain the following results:

$$\mathrm{BR}(K_S \to \pi^+\pi^-(\gamma)) = (69.196 \pm 0.024_{\mathrm{stat}} \pm 0.045_{\mathrm{syst}}) \times 10^{-2} \tag{38a}$$

$$\mathrm{BR}(K_S \to \pi^0\pi^0) = (30.687 \pm 0.024_{\mathrm{stat}} \pm 0.045_{\mathrm{syst}}) \times 10^{-2} \tag{38b}$$

$$\mathrm{BR}(K_S \to \pi^- e^+ \nu) = (3.528 \pm 0.057_{stat} \pm 0.027_{syst}) \times 10^{-4} \tag{38c}$$

$$\mathrm{BR}(K_S \to \pi^+ e^- \bar{\nu}) = (3.517 \pm 0.050_{stat} \pm 0.029_{syst}) \times 10^{-4} \tag{38d}$$

The mutual dependency of these estimates is described by the following correlation matrix for statistical and systematic errors:

$$\begin{array}{c} \\ \pi^+\pi^- \\ \pi^0\pi^0 \\ \pi^- e^+ \nu \\ \pi^+ e^- \overline{\nu} \end{array}
\begin{array}{c} \begin{array}{cccc} \pi^+\pi^- & \pi^0\pi^0 & \pi^- e^+ \nu & \pi^+ e^- \overline{\nu} \end{array} \\
\begin{pmatrix} 1 & -0.9986 & -0.0066 & -0.0010 \\ -0.9986 & 1 & -0.0335 & -0.0346 \\ -0.0066 & -0.0335 & 1 & -0.0007 \\ -0.0010 & -0.0346 & -0.0007 & 1 \end{pmatrix}_{\mathrm{stat}} \end{array}$$

$$\begin{array}{c} \pi^+\pi^- \\ \pi^0\pi^0 \\ \pi^- e^+ \nu \\ \pi^+ e^- \overline{\nu} \end{array}
\begin{pmatrix} 1 & -0.9998 & 0.0738 & 0.0673 \\ -0.9998 & 1 & -0.0902 & -0.0840 \\ 0.0738 & -0.0902 & 1 & 0.6159 \\ 0.0673 & -0.0840 & 0.6159 & 1 \end{pmatrix}_{\mathrm{syst}} \tag{39}$$

The correlation of the systematic errors between semileptonic BR's is due again to the tail correction uncertainty (see Eq. 29). The contribution from the error on $r_{\mu e}$ is included

	Fractional error (10^{-3})	
	Statistical	Systematic
Statistics of $K_S \to \pi e \nu$	9.1	
Statistics of $K_S \to \pi^+\pi^-(\gamma)$	0.1	
$K_S \to \pi e \nu$ selection		
DC preselection efficiency, TCA, T_0	1.5	2.9
Trigger	0.2	0.3
TOF	2.3	
Fit systematics		6.2
$K_S \to \pi^+\pi^-(\gamma)$selection		
DC preselection efficiency, TCA, T_0	0.3	1.6
Trigger	0.1	0.8
Ratio of tagging efficiencies	5.0	
Ratio of cosmic veto inefficiencies	1.0	
Total	10.8	7.1
Total relative error	**12.9**	
$\mathrm{BR}(K_S \to \pi^+\pi^-(\gamma))$		1.4

Table 17: Contributions to the fractional error on $\mathrm{BR}(K_S \to \pi e \nu)$.

in the systematic errors. The correlation matrix for the total errors is:

$$\begin{array}{c c} & \begin{array}{cccc} \pi^+\pi^- & \pi^0\pi^0 & \pi^-e^+\nu & \pi^+e^-\overline{\nu} \end{array} \\ \begin{array}{c} \pi^+\pi^- \\ \pi^0\pi^0 \\ \pi^-e^+\nu \\ \pi^+e^-\overline{\nu} \end{array} & \left(\begin{array}{cccc} 1 & -0.9996 & 0.0254 & 0.0294 \\ -0.9996 & 1 & -0.0484 & -0.0511 \\ 0.0254 & -0.0484 & 1 & 0.1320 \\ 0.0294 & -0.0511 & 0.1320 & 1 \end{array}\right)_{\mathrm{tot}} \end{array} \tag{40}$$

Taking into account the correlation matrix, for the total semileptonic BR we have:

$$\mathrm{BR}(K_S \to \pi e \nu) = (7.046 \pm 0.076_{stat} \pm 0.051_{syst}) \times 10^{-4} \tag{41}$$

The various contributions to the total fractional error on $\mathrm{BR}(K_S \to \pi e \nu)$ and to the total error on A_S are listed in table 17 and 18.

From the total BR shown in the right panel of Fig. 49 we can test the validity of the $\Delta S = \Delta Q$ rule. Comparing K_S and K_L semileptonich widths, we parametrize possible violations of the rule in the amplitudes conserving CPT as follows:

$$\Re(x_+) = \frac{1}{4}\left(\frac{\mathrm{BR}(K_S \to \pi e \nu)\tau_L}{\mathrm{BR}(K_L \to \pi e \nu)\tau_S} - 1\right) \tag{42}$$

	Error (10^{-3})	
	Statistical	Systematic
Statistics of $K_S \to \pi e \nu$	9.1	
$K_S \to \pi e \nu$ selection		
DC preselection efficiency, TCA, T_0	1.5	2.9
Trigger	0.1	0.3
TOF	2.3	
Fit systematics		0.4
Ratio of tagging efficiencies	0.4	
Ratio of cosmic veto inefficiencies	1.0	
Total	9.6	2.9
Total relative error	**10.0**	

Table 18: Contributions to the error on A_S.

We use the following values for the K_S and K_L lifetimes: $\tau_S = 0.08958(6)$ ns from PDG [13] and $\tau_L = 50.84(23)$ ns from recent measurements from KLOE [20, 19]. For the BR for $K_L \to \pi e \nu$, we compare the value from the KTeV experiment, 0.4067(11) [2], with that measured at KLOE, 0.4007(17) [20]. The corresponding values of $\Re(x_+)$ are shown in the right panels of Fig. 49. By combining the values from the analysis of year 2001 and 2002, we obtain the following results:

$$\Re(x_+)_{\mathrm{KTeV}} = \quad (-4.2 \pm 3.0_{stat} \pm 1.8_{syst}) \quad \times 10^{-3} \tag{43}$$

$$\Re(x_+)_{\mathrm{KLOE}} = \quad (-0.5 \pm 3.1_{stat} \pm 1.8_{syst}) \quad \times 10^{-3} \tag{44}$$

The errors are almost a factor of two smaller than the most precise measurement, from the CPLEAR experiment [5].

Finally, from the sum and difference of K_L and K_S charge asymmetries we can test for possible violations of the CPT symmetry, either in amplitudes or in the mass matrix. From the difference we obtain the following relation for the parameters $\Re(x_-)$ and $\Re(\Delta)$:

$$A_S - A_L = 4\Re(x_-) + 4\Re(\delta) \tag{45}$$

Using $A_L = (3.322 \pm 0.058_{\mathrm{stat}} \pm 0.047_{\mathrm{syst}})10^{-3}$ measured by the KTeV experiment [1], we obtain

$$\Re(x_-) + \Re(\delta) = (-0.5 \pm 2.4_{\mathrm{stat}} \pm 0.7_{\mathrm{syst}}) \times 10^{-3} \tag{46}$$

The knowledge of the two parameters is dominated by results from the CPLEAR experiment [6]: the error on $\Re(\delta)$ is 3×10^{-4} and that on $\Re(x_-)$ is 10^{-2}. Using the value

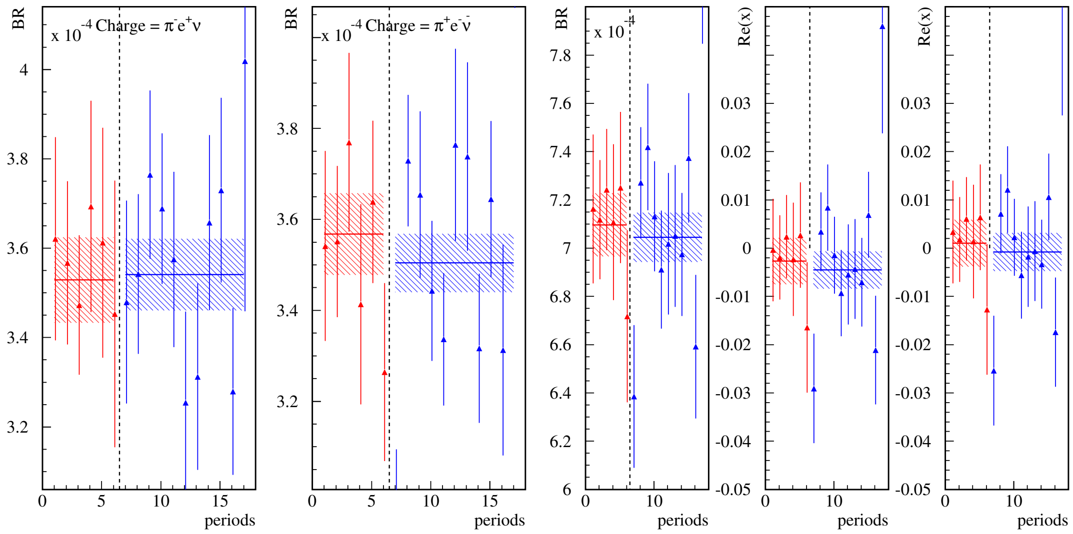

Figure 49: Left panels: results for the BR's $K_S \to \pi^- e^+ \nu$ and $K_S \to \pi^+ e^- \bar{\nu}$ as a function of the period along the data taking. Right panels: results for the total BR for $K_S \to \pi e \nu$ and for the $\Re(x_+)$ parameter obtained using the value of $\mathrm{BR}(K_L \to \pi e \nu)$ from KTeV (central panel) or KLOE (right panel) as a function of the period along the data taking. The horizontal bands represent the value for year 2001 (red) and 2002 (blue).

$\Re(\delta) = (3.0 \pm 3.3_{\rm stat} \pm 0.3_{\rm syst}) \times 10^{-4}$ from CPLEAR, we obtain:

$$\Re(x_-) = (-0.8 \pm 2.4_{\rm stat} \pm 0.7_{\rm syst}) \times 10^{-3}, \tag{47}$$

thus improving on the error of $\Re(x_-)$ by a factor of 10.

From the sum of the two asymmetries we have the relation

$$A_S + A_L = 4\Re(\epsilon) - 4\Re(y). \tag{48}$$

We then obtain

$$\Re(\epsilon) - \Re(y) = (1.2 \pm 2.4_{\rm stat} \pm 0.7_{\rm syst}) \times 10^{-3} \tag{49}$$

We calculate $\Re(\epsilon)$ from Ref. [13], without assuming CPT conservation: $\Re(\epsilon) = |\epsilon| \times \cos\phi_\epsilon = (1.62 \pm 0.04) \times 10^{-3}$. Subtracting this value from Eq. 49, we find

$$\Re(y) = (0.4 \pm 2.4_{\rm stat} \pm 0.7_{\rm syst}) \times 10^{-3} \tag{50}$$

compatible with the value obtained from unitary relation in Ref. [7].

6 $V_{\rm us}$ determination

The value of $V_{\rm us}$ can be extracted from the measurement of $\mathrm{BR}(K_S \to \pi^{\pm}e^{\mp}\bar{\nu}(\nu))$ and from the K_S lifetime, τ_S:

$$V_{\rm us}\ \times f_+^{K^0\pi^-}(0) = \left[\frac{128\pi^3\mathrm{BR}(K_S \to \pi^{\pm}e^{\mp}\bar{\nu}(\nu))}{\tau_S G_\mu^2 M_K^5 S_{\rm ew} I_K(\lambda_+, 0)}\right]^{1/2} \frac{1}{1+\delta_{\rm em}^K}, \tag{51}$$

where $f_+^{K^0\pi^-}$ is the vector form factor at zero momentum transfer and $I_K(\lambda_+,0)$ is the result of the phase space integration after factoring out $f_+^{K^0\pi^-}$; both quantities are evaluated in absence of radiative corrections. The radiative corrections [12, 4] for the form factor and the phase-space integral are included by the parameter $\delta_{\rm em}^K = (0.55 \pm 0.10) \times 10^{-2}$ [12]. The short-distance electroweak corrections are included in the parameter $S_{\rm ew} = 1.0232$ [23].

To evaluate $V_{\rm us}$ by Eq. (51), we use a quadratic parametrization of the vector form factor,

$$f_+(t) = f_+(0)\left[1 + \lambda'_+ \frac{t}{m_{\pi^2_+}} + \frac{\lambda''_+}{2}\frac{t^2}{m^4_{\pi^+}}\right],$$

which has been recently shown [3, 28] to be in better agreement with the data than the linear parametrization. We use the values $\lambda'_+ = 0.0221 \pm 0.0011$ and $\lambda''_+ = 0.0023 \pm 0.0004$, obtained from a combined fit to K_{e3} and $K_{\mu3}$ results from KTeV [3] and ISTRA+ [28]. With this parametrization, the integration over phase space yields $I_K(\lambda_+, 0) = 0.1024 \pm 0.0002$.

We obtain:

$$f_+^{K^0\pi^-} \times V_{\rm us}\ = 0.2162 \pm 0.0014$$

Using $V_{\rm ud} = 0.9738 \pm 0.0003$ from [24] and $f_+^{K^0\pi^-} = 0.961 \pm 0.008$ from [22] (where this latter value is in agreement with a recent lattice calculation [10]), the value expected on the basis of the first-raw CKM unitarity condition is:

$$\left(f_+^{K^0\pi^-} \times V_{\rm us}\right)_{\Delta=0} = 0.2185 \pm 0.0022$$

in agreement with our result.

Acknowledgements

References

[1] A. Alavi-Harati et al. *Phys. Rev. Lett.*, 88:181601, 2002. **hep-ex/0202016**.

[2] T. Alexopoulos et al. *Phys. Rev.*, D70:092006, 2004.

[3] T. Alexopoulos et al. *Phys. Rev.*, D70:092007, 2004. **hep-ex/0406003**.

[4] Troy C. Andre. Radiative corrections to K0(l3) decays,. 2004. **hep-ph/0406006**.

[5] A. Angelopoulos et al. *Phys. Lett.*, B444:38, 1998.

[6] A. Angelopoulos et al. *Phys. Lett.*, B444:52, 1998.

[7] A. Apostolakis et al. *Phys. Lett.*, B456:297, 1999.

[8] S. Baker and R. D. Cousins. *Nucl. Inst. Meth.*, A(221):437, 1984.

[9] R. J. Barlow and C. Beeston. Fitting using finite monte carlo samples. *Comput. Phys. Commun.*, 77:219–228, 1993.

[10] D. Becirevic et al. 2004. **hep-ph/0403217**.

[11] G. Cabibbo et al. The calibration of the space-time relations in the KLOE drift chamber. KLOE note 175 (2002).

[12] V. Cirigliano, H. Neufeld, and H. Pichl. *Eur. Phys. J.*, C35:53–65, 2004.

[13] S. Eidelman et al. Review of Particle Physics. *Physics Letters B*, 592, 2004. and 2005 partial update for edition 2006.

[14] C. Gatti. MC generators for radiative kaon decays. KLOE note 194 (2004).

[15] C. Gatti. Monte Carlo simulation for radiative kaon decays. *to be published in Eur. Phys. J. C*. **hep-ph/0507280**.

[16] C. Gatti. *Measurement of the branching fraction for the decay* $K_S \to \pi e \nu$. PhD thesis, Università degli Studi di Pisa, 2002.

[17] C. Gatti, M. Palutan, and T. Spadaro. Measurement of $\Gamma(K_S \to \pi^+\pi^-(\gamma))$/$\Gamma(K_S \to \pi^0\pi^0)$ with KLOE 2001-2002 data. KLOE note 209 (2006).

[18] C. Gatti and T. Spadaro. Measurement of $\mathrm{BR}(K \to \pi^{\pm}e^{\mp}\bar{\nu}(\nu))$. KLOE note 176 (2002).

[19] KLOE Collaboration. *Phys. Lett.*, B626:15, 2005. **hep-ex/0507088**.

[20] KLOE Collaboration. *Phys. Lett.*, B632:43, 2006. **hep-ex/0508027**.

[21] KTeV Collaboration. *Phys. Rev.*, D70:092007, 2004. **hep-ex/0406003**.

[22] H. Leutwyler and M. Roos. *Z. Phys.*, C25:91, 1984.

[23] William J. Marciano and A. Sirlin. *Phys. Rev. Lett.*, 71:3629–3632, 1993.

[24] William J. Marciano and Alberto Sirlin. Improved calculation of electroweak radiative corrections and the value of V(ud). 2005. **hep-ph/0510099**.

[25] T. Spadaro. Talk at La Thuile 2004.

[26] T. Spadaro. *Studies of Ks decays at the Kloe Experiment*. PhD thesis, Università degli Studi di Roma "La Sapienza", 2001.

[27] T. Spadaro et al. Performance of the KLOE calorimeter with DAPHNE data. In C. Cecchi, P. Cenci, P. Lubrano, M. Pepe, and World Scientific, editors, *Proceedings of the Eleventh International Conference on Calorimetry in Particle Physics, Perugia*, page 337, 2005.

[28] O. P. Yushchenko et al. *Phys. Lett.*, B589:111–117, 2004. **hep-ex/0404030**.